TVD and ENO Applications to Supersonic Flows in 3D – Part II

EDISSON SÁVIO DE GÓES MACIEL
IEA – Aeronautical Engineering Division
ITA – Aeronautical Technological Institute
Praça Mal. do Ar Eduardo Gomes, 50 – Vila das Acácias – São José dos Campos – SP – 12228-900
BRAZIL
edisavio@edissonsavio.eng.br http://www.edissonsavio.eng.br

Abstract: - In this work, second part of this study, the high resolution numerical schemes of Yee and Harten, of Yang second order, of Yang third order, and of Yang and Hsu are applied to the solution of the Euler and Navier-Stokes equations in three-dimensions. All schemes are flux difference splitting algorithms. The Yee and Harten is a TVD ("Total Variation Diminishing") second order accurate in space and first order accurate in time algorithm. The Yang second order is a TVD/ENO ("Essentially Nonoscillatory") second order accurate in space and first order accurate in time algorithm. The Yang third order is a TVD/ENO third order accurate in space and first order accurate in time algorithm. Finally, the Yang and Hsu is a UNO (Uniformly Nonoscillatory) third order accurate in space and first order accurate in time algorithm. The Euler and Navier-Stokes equations, written in a conservative and integral form, are solved, according to a finite volume and structured formulations. A spatially variable time step procedure is employed aiming to accelerate the convergence of the numerical schemes to the steady state condition. It has proved excellent gains in terms of convergence acceleration as reported by Maciel. The physical problems of the supersonic flows along a compression corner and along a ramp are solved, in the inviscid case. For the viscous case, the supersonic flow along a ramp is again solved. In the inviscid case, an implicit formulation is employed to marching in time, whereas in the viscous case, a time splitting or Strang approaches are used. The results have demonstrated that the Yang and Hsu UNO third order accurate algorithm has presented the best solutions in the problems studied herein. Moreover, it is also the best as comparing with the numerical schemes of Part I of this study.

Key-Words: - Yee and Harten algorithm, Yang second order TVD/ENO algorithm, Yang third order TVD/ENO algorithm, Yang and Hsu UNO algorithm, Euler and Navier-Stokes equations, Finite Volumes.

1 Introduction

In recent years, many high resolution shock capturing finite volume schemes for the computation of the Euler equations have been developed. Of special interest are the methods that generate nonoscillatory solutions but sharp approximations to shock and contact discontinuities. This interest stems from the fact that even with the advances in high-speed supercomputing, grid generation, automatic adaptive grid procedures, etc., the lack of robust and accurate numerical schemes is a major stumbling block for the success of computational fluid dynamics. Most of these schemes [1-9] are very different in form, methodology, and design principle. However, from the standpoint of numerical analysis, these schemes are total variation diminishing (TVD) for nonlinear scalar hyperbolic conservation laws and for constant coefficient hyperbolic systems. The notion of TVD schemes was introduced by Harten [1-2]. Some of these methods can also be viewed as three-point central difference schemes with a "smart" numerical dissipation or smoothing mechanism. "Smart" here means automatic feedback mechanism to control the amount of numerical dissipation for nonlinear problems. In general, TVD schemes can be divided into two categories, namely, upwind and symmetric TVD schemes. A way of distinguish an upwind from a symmetric TVD scheme is that the numerical dissipation term corresponding to an upwind TVD scheme is upwind-weighted [1-6] as opposed to the numerical dissipation term corresponding to a symmetric TVD scheme that is centered [7-9].

Harten's method of constructing high resolution TVD schemes involves starting with a first order TVD scheme and applying it to a modified flux. The modified flux is chosen so that the scheme is second order at regions of smoothness and first order at points of extrema. This technique is sometimes referred to as the modified flux approach. Although the scheme is an upwind scheme, it is written in a symmetric form; i.e., central difference plus an appropriate numerical dissipation term. This special form is especially advantageous for systems of higher than one space dimension. It results in less storage and a smaller operation count than its upwind form [10]. The modified flux approach is

relatively simple to understand and easy to implement into a new or existing computing code. One can modify a standard three-point central difference code by simply changing the conventional numerical dissipation term into the one designed for the TVD scheme.

In [11], a preliminary study was completed on the implicit TVD scheme for a two-dimensional gasdynamics problem in a Cartesian coordinate. It was found that further improvement in computation efficiency and converged rate is required for practical application.

[12] proposed a modification in the work of [11], written via the modified flux approach, aiming to extend these methods to the multidimensional hyperbolic conservation laws in curvilinear coordinates. They presented various ways of linearizing the implicit operator and solution strategies to improve the computation efficiency of the implicit algorithm were discussed. Numerical experiments with some AGARD test cases for steady-state airfoil calculations showed that the proposed linearized implicit upwind TVD schemes were quite robust and accurate.

Very recently, a new class of uniformly high-order-accurate essentially nonoscillatory (ENO) schemes have been developed by [13-15]. They presented a hierarchy of uniformly high-order-accurate schemes that generalize Godunov's scheme [16], its second order accurate MUSCL extension [3; 17] and the total variation diminishing (TVD) scheme [18] to arbitrary order of accuracy. In contrast to the earlier second-order TVD schemes which drop to first-order accuracy at local extrema and maintain second-order accuracy in smooth regions, the new ENO schemes are uniformly high-order accurate throughout, even at critical points. The ENO schemes use a reconstruction algorithm that is derived from a new interpolation technique that when applied to piecewise smooth data gives high-order accuracy whenever the function is smooth but avoids a Gibbs phenomenon at discontinuities. An adaptive stencil of grid points is used; therefore, the resulting schemes are highly nonlinear even in the scalar case.

Theoretical results for the scalar coefficient case and numerical results for the scalar conservation law and for the one-dimensional Euler equations of gas dynamics have been reported with highly accurate results. Such high-order ENO schemes have the potential to be adapted to the current Euler/Navier-Stokes flow solvers as one does for the second order TVD explicit and implicit schemes [11; 19-20] to further enhance the accuracy of flowfield simulation. Implementation can be either as a higher-order flow solver as in the present work or as a postprocessor to enhance the resolution.

[21] formally extended his second-order TVD schemes described in [22-23] to uniformly second-order ENO schemes for the two-dimensional Euler equations in curvilinear coordinate systems. Both explicit and implicit schemes were described. The authors emphasized in this work that TVD schemes are a special case of ENO schemes in which the TVD requirement is replaced by a less restricted essentially nonoscillatory condition, a concept advanced by Harten and co-workers [13-15]. Numerical experiments with the ENO scheme for an one-dimensional blast wave diffraction around a cylinder, shock wave collision over a circular arc, and steady transonic flow over a circular arc in a channel were reported.

[24] described a class of third-order, essentially nonoscillatory shock-capturing schemes for the Euler equations of gas dynamics. These schemes were obtained by applying the characteristic flux-difference splitting to an appropriately modified flux vector that could have high-order accuracy and nonoscillatory property. Third-order schemes were constructed using upstream interpolation and ENO interpolation. Both explicit and implicit schemes were derived. Implicit schemes to two-dimensional Euler equations in general coordinates were also given. The author applied the resulting schemes to simulate one-dimensional and two-dimensional unsteady shock tube flows and steady two-dimensional flows involving strong shocks to illustrate the performance of the schemes.

[25], following the works of [13-15], described a class of third-order (at least one-dimensional scalar case) shock capturing UNO schemes for the Euler equations of gas dynamics. Third-order schemes were constructing using UNO interpolation. The development was identical to those given in [24], except that Roe's approximate Riemann solver [26] was employed instead of the characteristic flux difference splitting method. The main difference between the approach used in [24] and in this work was that the former one operated on the difference of flux vector, whereas in this work operated on the difference of conservative state vector. It is known that the conservative vector is not continuous across the shock whereas the flux is continuous; that is, the flux vector function is one order smoother than the conservative state vector function. The Roe's averages [26] enable the Rankine-Hugoniot relations to be satisfied across the shock. Also, the Roe's linearization technique for nonlinear system permits the use of completely different characteristic

fields and is one of the most popular approximate Riemann solvers currently in use.

Traditionally, implicit numerical methods have been praised for their improved stability and condemned for their large arithmetic operation counts ([27]). On the one hand, the slow convergence rate of explicit methods become they so unattractive to the solution of steady state problems due to the large number of iterations required to convergence, in spite of the reduced number of operation counts per time step in comparison with their implicit counterparts. Such problem is resulting from the limited stability region which such methods are subjected (the Courant condition). On the other hand, implicit schemes guarantee a larger stability region, which allows the use of CFL (Currant-Friedrichs-Lewis) numbers above 1.0, and fast convergence to steady state conditions. Undoubtedly, the most significant efficiency achievement for multidimensional implicit methods was the introduction of the Alternating Direction Implicit (ADI) algorithms by [28-30], and fractional step algorithms by [31]. ADI approximate factorization methods consist in approximating the Left Hand Side (LHS) of the numerical scheme by the product of one-dimensional parcels, each one associated with a different spatial coordinate direction, which retract nearly the original implicit operator. These methods have been largely applied in the CFD ("Computational Fluid Dynamics") community and, despite the fact of the error of the approximate factorization, it allows the use of large time steps, which results in significant gains in terms of convergence rate in relation to explicit methods.

In the present work, second part of this study, the [12] TVD, the [21] TVD/ENO, the [24] TVD/ENO, and the [25] UNO schemes are implemented, on a finite volume context and using a structured spatial discretization, to solve the Euler and Navier-Stokes equations in the three-dimensional space. All schemes are high resolution flux difference splitting ones, based on the concept of Harten's modified flux function. The [12] is a TVD second order accurate in space and first order accurate in time algorithm. [21] is a TVD/ENO second order accurate in space and first order accurate in time algorithm. The [24] is a TVD/ENO third order accurate in space and first order accurate in time algorithm. Finally, the [25] is a UNO (Uniformly Nonoscillatory) third order accurate in space and first order accurate in time algorithm. An implicit formulation is employed to solve the Euler equations, whereas a time splitting or Strang methods, explicit methods, are used to solve the Navier-Stokes equations. A Linearized Nonconservative Implicit LNI form or an approximate factorization ADI method is employed by the schemes. The algorithms are accelerated to the steady state solution using a spatially variable time step, which has demonstrated effective gains in terms of convergence rate ([32-33]). All schemes are applied to the solution of physical problems of the supersonic flows along a compression corner and along a ramp, in the inviscid case. For the viscous case, the supersonic flow along a ramp is again solved. The results have demonstrated that the [25] UNO algorithm, third order accurate in space, has presented the best solutions, in this study.

2 Navier-Stokes Equations

As the Euler equations can be obtained from the Navier-Stokes ones by disregarding the viscous vectors, only the formulation to the latter will be presented. The Navier-Stokes equations in integral conservative form, employing a finite volume formulation and using a structured spatial discretization, to three-dimensional simulations, are written as:

$$\partial Q/\partial t + 1/V \int_V \vec{\nabla} \cdot \vec{P} dV = 0 \,, \qquad (1)$$

where V is the cell volume, which corresponds to an hexahedron in the three-dimensional space; Q is the vector of conserved variables; and $\vec{P} = (E_e - E_v)\vec{i} + (F_e - F_v)\vec{j} + (G_e - G_v)\vec{k}$ represents the complete flux vector in Cartesian coordinates, with the subscript "e" related to the inviscid contributions or the Euler contributions and "v" is related to the viscous contributions. These components of the complete flux vector, as well the vector of conserved variables, are defined as:

$$Q = \begin{Bmatrix} \rho \\ \rho u \\ \rho v \\ \rho w \\ e \end{Bmatrix}, \; E_e = \begin{Bmatrix} \rho u \\ \rho u^2 + p \\ \rho uv \\ \rho uw \\ (e+p)u \end{Bmatrix}, \; F_e = \begin{Bmatrix} \rho v \\ \rho uv \\ \rho v^2 + p \\ \rho vw \\ (e+p)v \end{Bmatrix} G_e = \begin{Bmatrix} \rho w \\ \rho uw \\ \rho vw \\ \rho w^2 + p \\ (e+p)w \end{Bmatrix}; \quad (2)$$

$$E_v = \frac{1}{\mathrm{Re}} \begin{Bmatrix} 0 \\ \tau_{xx} \\ \tau_{xy} \\ \tau_{xz} \\ \tau_{xx}u + \tau_{xy}v + \tau_{xz}w - q_x \end{Bmatrix}, \; F_v = \frac{1}{\mathrm{Re}} \begin{Bmatrix} 0 \\ \tau_{xy} \\ \tau_{yy} \\ \tau_{yz} \\ \tau_{xy}u + \tau_{yy}v + \tau_{yz}w - q_y \end{Bmatrix}; \quad (3a)$$

$$G_v = \frac{1}{\mathrm{Re}} \begin{Bmatrix} 0 \\ \tau_{xz} \\ \tau_{yz} \\ \tau_{zz} \\ \tau_{xz}u + \tau_{yz}v + \tau_{zz}w - q_z \end{Bmatrix} \quad (3b)$$

In these equations, the components of the viscous stress tensor are defined as:

$$\tau_{xx} = 2\mu_M \partial u/\partial x - 2/3\mu_M(\partial u/\partial x + \partial v/\partial y + \partial w/\partial z); \quad (4)$$

$$\tau_{xy} = \mu_M(\partial u/\partial y + \partial v/\partial x); \quad (5)$$

$$\tau_{xz} = \mu_M(\partial w/\partial x + \partial u/\partial z); \quad (6)$$

$$\tau_{yy} = 2\mu_M \partial v/\partial y - 2/3\mu_M(\partial u/\partial x + \partial v/\partial y + \partial w/\partial z); \quad (7)$$

$$\tau_{yz} = \mu_M(\partial v/\partial z + \partial w/\partial y); \quad (8)$$

$$\tau_{zz} = 2\mu_M \partial w/\partial z - 2/3\mu_M(\partial u/\partial x + \partial v/\partial y + \partial w/\partial z). \quad (9)$$

The components of the conductive heat flux vector are defined as follows:

$$q_x = -\gamma(\mu_M / Pr\, d)\partial e_i/\partial x; \quad (10)$$

$$q_y = -\gamma(\mu_M / Pr\, d)\partial e_i/\partial y; \quad (11)$$

$$q_z = -\gamma(\mu_M / \mathrm{Pr}\, d)\partial e_i/\partial z. \quad (12)$$

The quantities that appear above are described as follows: ρ is the fluid density, *u v* and w are the Cartesian components of the flow velocity vector in the *x*, *y* and z directions, respectively; *e* is the total energy per unit volume of the fluid; *p* is the fluid static pressure; e_i is the fluid internal energy, defined as:

$$e_i = e/\rho - 0.5(u^2 + v^2 + w^2); \quad (13)$$

the τ's represent the components of the viscous stress tensor; Prd is the laminar Prandtl number, which assumed a value of 0.72 in the present simulations; the *q*'s represent the components of the conductive heat flux; μ_M is the fluid molecular viscosity; γ is the ratio of specific heats at constant pressure and volume, respectively, which assumed a value 1.4 to the atmospheric air; and Re is the Reynolds number of the viscous simulation, defined by:

$$\mathrm{Re} = \rho u_{REF} l/\mu_M, \quad (14)$$

where u_{REF} is a characteristic flow velocity and *l* is a configuration characteristic length. The molecular viscosity is estimated by the empiric Sutherland formula:

$$\mu_M = bT^{1/2}/(1 + S/T), \quad (15)$$

where T is the absolute temperature (K), b = $1.458\text{x}10^{-6}$ Kg/(m.s.$K^{1/2}$) and S = 110.4 K, to the atmospheric air in the standard atmospheric conditions ([34]). The Navier-Stokes equations were dimensionless in relation to the freestream density, ρ_∞, and the freestream speed of sound, a_∞, for the all problems. For the viscous ramp problem it is also considered the freestream molecular viscosity, μ_∞. To allow the solution of the matrix system of five equations to five unknowns described by Eq. (1), it is employed the state equation of perfect gases presented below:

$$p = (\gamma - 1)\left[e - 0.5\rho(u^2 + v^2 + w^2)\right]. \quad (16)$$

The total enthalpy is determined by:

$$H = (e + p)/\rho. \quad (17)$$

3 Yee and Harten TVD Second Order Algorithm

The [12] TVD algorithm, second order accurate in space, is specified by the determination of the numerical flux vector at the *(i+½,j,k)* interface. The extension of this numerical flux to the *(i,j+½,k)* and *(i,j,k+½)* interfaces is straightforward, without any additional complications.

The right and left cell volumes, as well the interface volume, necessary to coordinate change, following the finite volume formulation, which is equivalent to a generalized coordinate system, are defined as:

$$V_R = V_{i+1,j,k},\ V_L = V_{i,j,k} \text{ and } V_{\mathrm{int}} = 0.5(V_R + V_L), \quad (18)$$

where "R" and "L" represent right and left, respectively. The cell volume, the computational cell and its interface surfaces are defined in [35-36].

The area components at interface are defined by: $S_{x\_\mathrm{int}} = n_x S$, $S_{y\_\mathrm{int}} = n_y S$, and $S_{z\_\mathrm{int}} = n_z S$ where n_x, n_y and n_z are normal unity vector components. Expressions to these components and to the flux

area, *S*, are given in [35-36]. The metric terms to this generalized coordinate system are defined as:

$$h_x = S_{x\_\text{int}}/V_{\text{int}}\ ,\ h_y = S_{y\_\text{int}}/V_{\text{int}}\ ,\ h_z = S_{z\_\text{int}}/V_{\text{int}}\ ;$$
$$h_n = S/V_{\text{int}}\ . \qquad (19)$$

The calculated properties at the flux interface are obtained by arithmetical average or by Roe's average. The Roe's average was used in this work:

$$\rho_{\text{int}} = \sqrt{\rho_L \rho_R}\ ,\ u_{\text{int}} = \left(u_L + u_R\sqrt{\rho_R/\rho_L}\right)\Big/\left(1+\sqrt{\rho_R/\rho_L}\right), \qquad (20)$$
$$v_{\text{int}} = \left(v_L + v_R\sqrt{\rho_R/\rho_L}\right)\Big/\left(1+\sqrt{\rho_R/\rho_L}\right); \qquad (21)$$
$$w_{\text{int}} = \left(w_L + w_R\sqrt{\rho_R/\rho_L}\right)\Big/\left(1+\sqrt{\rho_R/\rho_L}\right); \qquad (22)$$
$$H_{\text{int}} = \left(H_L + H_R\sqrt{\rho_R/\rho_L}\right)\Big/\left(1+\sqrt{\rho_R/\rho_L}\right); \qquad (23)$$
$$a_{\text{int}} = \sqrt{(\gamma-1)\left[H_{\text{int}} - 0.5\left(u_{\text{int}}^2 + v_{\text{int}}^2 + w_{\text{int}}^2\right)\right]}\ . \qquad (24)$$

The eigenvalues of the Euler equations, in the ξ direction, to the convective flux are given by:

$$U_{cont} = u_{\text{int}}h_x + v_{\text{int}}h_y + w_{\text{int}}h_z\ ,\ \lambda_1 = U_{cont} - a_{\text{int}}h_n\ , \qquad (25)$$
$$\lambda_2 = \lambda_3 = \lambda_4 = U_{cont} \quad \text{and} \quad \lambda_5 = U_{cont} + a_{\text{int}}h_n\ . \qquad (26)$$

The jumps in the conserved variables, necessary to the construction of the [12] TVD dissipation function, are given by:

$$\Delta e = V_{\text{int}}(e_R - e_L),\ \Delta\rho = V_{\text{int}}(\rho_R - \rho_L),\ \Delta(\rho u) = V_{\text{int}}\left[(\rho u)_R - (\rho u)_L\right]; \qquad (27)$$
$$\Delta(\rho v) = V_{\text{int}}\left[(\rho v)_R - (\rho v)_L\right]\ \Delta(\rho w) = V_{\text{int}}\left[(\rho w)_R - (\rho w)_L\right]. \qquad (28)$$

The α vectors to the *(i+½,j,k)* interface are calculated by the following expression:

$$\{\alpha\}_{i+1/2,j,k} = [R]^{-1}_{i+1/2,j,k}\,\Delta Q_{i+1/2,j,k}\ , \qquad (29)$$

with $[R]^{-1}_{i+1/2,j,k}$ being defined in [35-36] and ΔQ being the jump of conserved variables. The [12] TVD dissipation function is constructed using the right eigenvector matrix of the Jacobian matrix in the normal direction to the flux face. This matrix is defined in [35-36].

The numerical flux function or modified function of [1], g, responsible to the second order accuracy of the [12] scheme, is defined as:

$$g^l_{i,j,k} = S \times MAX\left[0, MIN\left(\left|\alpha^l_{i+1/2,j,k}\right|, S\times\alpha^l_{i-1/2,j,k}\right)\right] \qquad (30)$$

with:

$$S = sign\left(\alpha^l_{i+1/2,j,k}\right). \qquad (31)$$

The entropy function to avoid non-physical solutions, is defined as:

$$\Psi(z) = \begin{cases} |z| & if \quad |z| \geq \varepsilon \\ \left(z^2 + \varepsilon^2\right)/(2\varepsilon) & if \quad |z| < \varepsilon \end{cases} \qquad (32)$$

with ε = 0.2, as recommended by [11].

The numerical information propagation velocity, φ, responsible to transport the numerical information to the algorithm, is determined by:

$$\phi^l_{i+1/2,j,k} = \frac{1}{2}\Psi\left(\lambda^l_{i+1/2,j,k}\right)\times\begin{cases}\left(g^l_{i+1,j,k} + g^l_{i,j,k}\right)/\alpha^l_{i+1/2,j,k} & if \quad \alpha_{i+1/2,j,k} \neq 0.0 \\ 0.0 & if \quad \alpha^l_{i+1/2,j,k} = 0.0\end{cases}. \qquad (33)$$

The ϕ dissipation function to form the numerical dissipation operator is written as

$$\phi^l_{i+1/2,j,k} = \frac{1}{2}\Psi\left(\lambda^l_{i+1/2,j,k}\right)\left(g^l_{i,j,k} + g^l_{i+1,j,k}\right) - \Psi\left(\lambda^l_{i+1/2,j,k} + \phi^l_{i+1/2,j,k}\right)\alpha^l_{i+1/2,j,k}\ . \qquad (34)$$

In Equations (30-34), "*l*" varies from 1 to 5 (three-dimensional space), in all definitions.

Finally, the [12] TVD dissipation function is constructed by the following matrix-vector product:

$$\{D_{YH}\}_{i+1/2,j,k} = [R]_{i+1/2,j,k}\{\Phi\}_{i+1/2,j,k}\ , \qquad (35)$$

with $[R]_{i+1/2,j,k}$ defined in [35-36].

The complete numerical flux vector to the *(i+½,j,k)* interface is described by:

$$F^{(l)}_{i+1/2,j,k} = \left(E^{(l)}_{\text{int}}h_x + F^{(l)}_{\text{int}}h_y + G^{(l)}_{\text{int}}h_z\right)V_{\text{int}} + 0.5D^{(l)}_{YH}, \qquad (36)$$

with:

$$E^{(l)}_{\text{int}} = 0.5\left[\left(E^{(l)}_R + E^{(l)}_L\right)_e\right] - \left(E^{(l)}_v\right)_{\text{int}}; \qquad (37)$$
$$F^{(l)}_{\text{int}} = 0.5\left[\left(F^{(l)}_R + F^{(l)}_L\right)_e\right] - \left(F^{(l)}_v\right)_{\text{int}}; \qquad (38)$$
$$G^{(l)}_{\text{int}} = 0.5\left[\left(G^{(l)}_R + G^{(l)}_L\right)_e\right] - \left(G^{(l)}_v\right)_{\text{int}}. \qquad (39)$$

The viscous vectors at the flux interface are obtained by arithmetical average between the primitive variables at the left and at the right states of the flux interface, as also arithmetical average of

the primitive variable gradients also considering the left and the right states of the flux interface.

The right-hand-side (RHS) of the [12] TVD scheme, necessaries to the resolution of the implicit version of this algorithm, is determined by:

$$RHS(YH)^n_{i,j,k} = -\Delta t_{i,j,k} / V_{i,j,k} \left(F^{YH}_{i+1/2,j,k} - F^{YH}_{i-1/2,j,k} + F^{YH}_{i,j+1/2,k} - F^{YH}_{i,j-1/2,k} + F^{YH}_{i,j,k+1/2} - F^{YH}_{i,j,k-1/2} \right)^n . \quad (40)$$

The time integration to the viscous simulations follows the time splitting method, first order accurate, which divides the integration in three steps, each one associated with a specific spatial direction. In the initial step, it is possible to write for the ξ direction:

$$\Delta Q^*_{i,j,k} = -\Delta t_{i,j,k} / V_{i,j,k} \left(F^n_{i+1/2,j,k} - F^n_{i-1/2,j,k} \right); \quad Q^*_{i,j,k} = Q^n_{i,j,k} + \Delta Q^*_{i,j,k}; \quad (41)$$

at the intermediate step, η direction:

$$\Delta Q^{**}_{i,j,k} = -\Delta t_{i,j,k} / V_{i,j,k} \left(F^*_{i,j+1/2,k} - F^*_{i,j-1/2,k} \right); \quad Q^{**}_{i,j,k} = Q^*_{i,j,k} + \Delta Q^{**}_{i,j,k}; \quad (42)$$

and at the end step, ζ direction:

$$\Delta Q^{n+1}_{i,j,k} = -\Delta t_{i,j,k} / V_{i,j,k} \left(F^{**}_{i,j,k+1/2} - F^{**}_{i,j,k-1/2} \right); \quad Q^{n+1}_{i,j,k} = Q^{**}_{i,j,k} + \Delta Q^{n+1}_{i,j,k}. \quad (43)$$

4 Yang TVD/ENO Second Order Algorithm

A typical conservative numerical scheme, using a finite volume formulation, for solving Eq. (1) can be expressed in terms of numerical fluxes as follows:

$$Q^{n+1}_{i,j,k} = Q^n_{i,j,k} - \frac{\Delta t_{i,j,k}}{V_{i,j,k}} \left(E^N_{i+1/2,j,k} - E^N_{i-1/2,j,k} \right) - \frac{\Delta t_{i,j,k}}{V_{i,j,k}} \left(F^N_{i,j+1/2,k} - F^N_{i,j-1/2,k} \right) - \frac{\Delta t_{i,j,k}}{V_{i,j,k}} \left(G^N_{i,j,k+1/2} - G^N_{i,j,k-1/2} \right), \quad (44)$$

where $E^N_{i+1/2,j,k}$, $F^N_{i,j+1/2,k}$ and $G^N_{i,j,k+1/2}$ are the numerical fluxes. For a first order upwind scheme, $E^N_{i+1/2,j,k}$ is given by:

$$E^N_{i+1/2,j,k} = E^n_{i+1/2,j,k} - \hat{A}^+_{i+1/2,j,k} \Delta_{i+1/2,j,k} E^n_{i,j,k}, \quad (45)$$

with: $\Delta_{i+1/2,j,k} = (\cdot)_{i+1,j,k} - (\cdot)_{i,j,k}$, $E^n_{i+1/2,j,k}$ and $E^n_{i,j,k}$ defined by:

$$E^n_{i+1/2,j,k} = V_{\text{int}} \begin{Bmatrix} \rho U_{cont} \\ \rho u U_{cont} + p h_x \\ \rho v U_{cont} + p h_y \\ \rho w U_{cont} + p h_z \\ (e+p) U_{cont} \end{Bmatrix}^n_{i+1/2,j,k}$$

and

$$E^n_{i,j,k} = V_{\text{int}} \begin{Bmatrix} \rho U_{cont} \\ \rho u U_{cont} + p h_x \\ \rho v U_{cont} + p h_y \\ \rho w U_{cont} + p h_z \\ (e+p) U_{cont} \end{Bmatrix}^n_{i,j,k} \quad (46)$$

and $\hat{A}^+_{i+1/2,j,k}$ defined as follows:

$$\hat{A}^+_{i+1/2,j,k} = \left(R_\xi \hat{\Lambda}^+_\xi R^{-1}_\xi \right)_{i+1/2,j,k}, \quad (47a)$$

$$\hat{\Lambda}^+_\xi = diag\left\{ \hat{\lambda}^+_l \right\} \text{ and } \hat{\lambda}^+_l = 0.5\left[1 + sign\left(\lambda^\xi_l \right) \right], \quad (47b)$$

where: $diag(\cdot)$ represents a diagonal matrix, as for instance:

$$\hat{\Lambda}^+_\xi = \begin{bmatrix} \hat{\lambda}^+_1 & & & & \\ & \hat{\lambda}^+_2 & & & \\ & & \hat{\lambda}^+_3 & & \\ & & & \hat{\lambda}^+_4 & \\ & & & & \hat{\lambda}^+_5 \end{bmatrix}; \quad (48)$$

λ^ξ_l are defined by Eqs. (25-26) to the ξ direction; $sign\left(\lambda^\xi_l \right)$ is equal to 1.0 if $\lambda^\xi_l \geq 0.0$ and -1.0 otherwise.

4.1 Uniformly second order essentially non-oscillatory scheme

[1] proposed to construct second order accurate TVD schemes by applying a first order approximate Riemann solver to a modified flux. Following [1], [21] proposed to define a modified numerical flux function with the definition of the modified fluxes:

$$E^n = E^M = E^n + \overline{E}^n;$$
$$F^n = F^M = F^n + \overline{F}^n;$$
$$G^n = G^M = G^n + \overline{G}^n, \quad (49)$$

where E^M, F^M and G^M are the modified fluxes which have essentially non-oscillatory property yet to be defined. In the following, a numerical method of uniformly second order accuracy in time and space which combines both characteristic and conversion features of Eq. (1) is discussed.

For the present ENO scheme, the numerical flux E^N is described by:

$$E^N_{i+1/2,j,k} = E^M_{i+1,j,k} - \hat{A}^+_{\xi_{i+1/2,j,k}} \Delta_{i+1/2,j,k} E^M_{i,j,k} = E^M_{i,j,k} + \hat{A}^-_{\xi_{i+1/2,j,k}} \Delta_{i+1/2,j,k} E^M_{i,j,k}. \quad (50)$$

The components of the additional vector $\overline{E}$ are given by:

$$\overline{e}_{i,j,k} = m\left[\tilde{e}_{i-1/2,j,k} + \beta\overline{m}\left(\Delta_- \tilde{e}_{i-1/2,j,k}, \Delta_+ \tilde{e}_{i-1/2,j,k}\right), \tilde{e}_{i+1/2,j,k} - \beta\overline{m}\left(\Delta_- \tilde{e}_{i+1/2,j,k}, \Delta_+ \tilde{e}_{i+1/2,j,k}\right)\right], \quad (51)$$

where:

$$\Delta_- = (\cdot)_{i,j,k} - (\cdot)_{i-1,j,k}, \ \Delta_+ = (\cdot)_{i+1,j,k} - (\cdot)_{i,j,k}; \quad (52)$$

and $\tilde{e}_{i+1/2,j,k}$ are components of the following column vector:

$$\tilde{E}_{i+1/2,j,k} = sign\left(A_{i+1/2,j,k}\right)\left(I - \Delta t_{i,j,k}\left|A_{i+1/2,j,k}\right|\right) \Delta_{i+1/2,j,k} E_{i,j,k}/2. \quad (53)$$

The $sign(A)$ and $|A|$ in Eq. (53) are given by:

$$sign(A) = R_\xi \, diag\left\{sign\left(\lambda^\xi_l\right)\right\} R^{-1}_\xi;$$
$$|A| = R_\xi \, diag\left\{\left|\lambda^\xi_l\right|\right\} R^{-1}_\xi. \quad (54)$$

Similar derivations can be given for the $\overline{F}$ and $\overline{G}$ vectors in the η and ζ directions. In Equation (51), m is the minmod function:

$$m(a,b) = \begin{cases} s \times \min\left(|a|,|b|\right) & if \quad sign(a) = sign(b) = s \\ 0.0 & otherwise \end{cases}; \quad (55)$$

and the $\overline{m}$ function is defined by:

$$\overline{m} = \begin{cases} a & if \quad |a| \le |b| \\ b & if \quad |a| \ge |b| \end{cases}. \quad (56)$$

For β = 0.0, one has a second order TVD scheme. For β = 0.5, one has a uniformly second order non-oscillatory scheme. The original numerical scheme of [21] is thus formed by Eq. (44) using the definition (50) to the numerical flux function.

The present author introduced some modifications in the [21] scheme in this work. Equation (50) is redefined as:

$$E^N_{i+1/2,j,k} = E^M_{i+1,j,k} - A^+_{\xi_{i+1/2,j,k}} \Delta_{i+1/2,j,k} Q^M_{i,j,k} = E^M_{i,j,k} + A^-_{\xi_{i+1/2,j,k}} \Delta_{i+1/2,j,k} Q^M_{i,j,k}, \quad (57)$$

with:

$$E^M_{i+1,j,k} = E^n_{i+1,j,k} + A^n_{\xi_{i,j,k}} \overline{E}^n_{i+1,j,k}; \quad (58)$$

$$Q^M_{i,j,k} = V_{\text{int}} \begin{Bmatrix} \rho \\ \rho u \\ \rho v \\ \rho w \\ e \end{Bmatrix}_{i,j,k} + \overline{E}^n_{i,j,k}. \quad (59)$$

The positive splitting matrix $A^+_{\xi_{i+1/2,j,k}}$ is defined as

$$A^+_{\xi_{i+1/2,j,k}} = R_\xi \, diag\left\{\lambda^+_l\right\} R^{-1}_\xi, \quad (60)$$

with:

$$\lambda^+_l = 0.5\left(\lambda^\xi_l + \left|\lambda^\xi_l\right|\right), \quad (61)$$

and the Jacobian matrix at the ξ direction is described by

$$A^n_{\xi_{i,j}} = R_\xi \, diag\left\{\lambda^\xi_l\right\} R^{-1}_\xi. \quad (62)$$

The vector $\tilde{E}_{i+1/2,j,k}$ is also redefined as:

$$\tilde{E}_{i+1/2,j,k} = sign\left(A_{i+1/2,j,k}\right)\left(I - \Delta t_{i,j,k}\left|A_{i+1/2,j,k}\right|\right) \Delta_{i+1/2,j,k} Q_{i,j,k}/2, \quad (63)$$

where:

$$Q_{i,j,k} = V_{\text{int}} \left\{\rho \quad \rho u \quad \rho v \quad \rho w \quad e\right\}^T_{i,j,k}. \quad (64)$$

Observe that the resulting scheme is equivalent to the original of [21], with the unique difference that

the difference of fluxes in Eq. (53) is changed by the difference of conserved variables. With this new definition, the solutions present better behaviour, free of oscillations, undershoots and overshoots. The other expressions maintain the same structure.

The right-hand-side of the [21] scheme, necessaries to the resolution of the implicit version of this algorithm, is defined by:

$$RHS(Y)^n_{i,j,k} = -\frac{\Delta t_{i,j,k}}{V_{i,j,k}}\left(E^N_{i+1/2,j,k} - E^N_{i-1/2,j,k}\right) - \frac{\Delta t_{i,j,k}}{V_{i,j,k}}\left(F^N_{i,j+1/2,k} - F^N_{i,j-1/2,k}\right) - \frac{\Delta t_{i,j,k}}{V_{i,j,k}}\left(G^N_{i,j,k+1/2} - G^N_{i,j,k-1/2}\right). \quad (65)$$

The viscous formulation obeys the same procedure described in section 3. For explicit methods in three-dimensions, the Strang-type directional splitting [37] was employed

$$Q^{n+2}_{i,j,k} = L_\xi(\Delta t)L_\eta(\Delta t)L_\zeta(\Delta t)L_\zeta(\Delta t)L_\eta(\Delta t)L_\xi(\Delta t)Q^n_{i,j,k} \quad (66)$$

The L_ξ operator is defined by

$$L_\xi(\Delta t)Q^n_{i,j,k} = Q^n_{i,j,k} - \Delta t_{i,j,k}\left(E^N_{i+1/2,j,k} - E^N_{i-1/2,j,k}\right). \quad (67)$$

Similar expressions can be given for $F^N_{i,j+1/2,k}$ and the L_η operator and for $G^N_{i,j,k+1/2}$ and L_ζ.

5 Yang TVD/ENO Third Order Algorithm

5.1 TVD formulation

In [38], second- and third-order upwind schemes have been described by one-dimensional cases. It was found that such high-order schemes can be constructed by using a more accurate flux representation (in the discrete sense) at each nodal point. [24] has taken such an approach following Harten's work [18] in which he applied a three-point first-order upwind scheme to a modified flux to yield second-order TVD scheme. Therefore, [24] calls it the modified flux approach.

[24] has considered a high-order extension of the Euler equations in one-dimensional case. The extension to the three-dimensional case is as follows:

$$\frac{\partial Q}{\partial t} + \left(\hat{A}^+ + \hat{A}^-\right)\frac{\partial E^M(Q)}{\partial x} + \left(\hat{B}^+ + \hat{B}^-\right)\frac{\partial F^M(Q)}{\partial y} + \quad (68a)$$

$$\left(\hat{C}^+ + \hat{C}^-\right)\frac{\partial G^M(Q)}{\partial z} = 0. \quad (68b)$$

Here, $E^M_{i,j,k}$, $F^M_{i,j,k}$ and $G^M_{i,j,k}$ are called the modified flux vectors at nodal point (i,j,k) and is consisted of the original flux vectors $E_{i,j,k}$, $F_{i,j,k}$ and $G_{i,j,k}$ and additional terms of high-order accuracy that usually have some nonlinear control terms to avoid oscillatory solutions.

In terms of numerical flux vector, a conservative scheme for Eq. (68) could be Eq. (44), with the numerical flux, in the ξ direction, defined as:

$$E^N_{i+1/2,j,k} = E^M_{i+1,j,k} - \hat{A}^+_{i+1/2,j,k}\Delta_+ E^M_{i,j,k} = E^M_{i,j,k} + \hat{A}^-_{i+1/2,j,k}\Delta_+ E^M_{i,j,k}. \quad (69)$$

A third-order scheme for Eq. (44) can be expressed in terms of numerical flux of the form Eq. (69) with

$$E^M_{i,j,k} = E^{TVD3}_{i,j,k} = E^n_{i,j,k} + D^n_{i,j,k}. \quad (70)$$

The components of $D_{i,j,k}$ are given by

$$d^l_{i,j,k} = \left[1 - S\left(\theta^l_{i,j,k}\right)\right]\tilde{d}^l_{i+1/2,j,k} + \left[1 + S\left(\theta^l_{i,j,k}\right)\right]\bar{d}^l_{i-1/2,j,k}, \quad (71)$$

where $\tilde{d}^l_{i+1/2,j,k}$ and $\bar{d}^l_{i+1/2,j,k}$ are components of $\tilde{D}_{i+1/2,j,k}$ and $\bar{D}_{i+1/2,j,k}$ given, respectively, by

$$\tilde{D}_{i+1/2,j,k} = signA_{i+1/2,j,k}\left(\Delta t^2_{i,j,k}\left|A_{i+1/2,j,k}\right|^2 - 3\Delta t_{i,j,k}\left|A_{i+1/2,j,k}\right| + 2I\right)\Delta_+ E_{i,j,k}/6; \quad (72)$$

$$\bar{D}_{i+1/2,j,k} = signA_{i+1/2,j,k}\left(I - \Delta t^2_{i,j,k}\left|A_{i+1/2,j,k}\right|^2\right), \quad \Delta_+ E_{i,j,k}/6 \quad (73)$$

and $S\left(\theta^l_{i,j,k}\right)$ is the smoothness monitor given by [39] as

$$S\left(\theta^{l}_{i,j,k}\right)=\begin{cases}0, & if \quad \left|\Delta_{+}q^{l}_{i,j,k}\right|+\left|\Delta_{-}q^{l}_{i,j,k}\right|=0\\ \dfrac{\left|\Delta_{+}q^{l}_{i,j,k}\right|-\left|\Delta_{-}q^{l}_{i,j,k}\right|}{\left|\Delta_{+}q^{l}_{i,j,k}\right|+\left|\Delta_{-}q^{l}_{i,j,k}\right|}, & otherwise\end{cases}; \quad (74)$$

where $q^{l}_{i,j,k}$ are components of the conservative state vector $Q_{i,j,k}$; and the Δ's defined as follows to the ξ direction:

$$\Delta_{+}=(\cdot)_{i+1,j,k}-(\cdot)_{i,j,k} \text{ and } \Delta_{-}=(\cdot)_{i,j,k}-(\cdot)_{i-1,j,k}. \quad (75)$$

The present author of this work introduces some modifications in the original scheme of [24]. These modifications are as follows:

$$E^{N}_{i+1/2,j,k}=E^{M}_{i+1,j,k}-A_{\xi_{i+1/2,j,k}}\Delta_{+}Q^{M}_{i,j,k}, \quad (76)$$

where:

$$Q^{M}_{i,j,k}=V_{\text{int}}\begin{Bmatrix}\rho\\ \rho u\\ \rho v\\ \rho w\\ e\end{Bmatrix}+D^{n}_{i,j,k}; \quad (77)$$

$$E^{M}_{i,j,k}=E^{n}_{i,j,k}+A^{n}_{\xi_{i,j,k}}D^{n}_{i,j,k}; \quad (78)$$

$$\tilde{D}_{i+1/2,j,k}=signA_{i+1/2,j,k}\left(\Delta t^{2}_{i,j,k}\left|A_{i+1/2,j,k}\right|^{2}-3\Delta t_{i,j,k}\left|A_{i+1/2,j,k}\right|+2I\right)\Delta_{+}Q_{i,j,k}/6; \quad (79)$$

$$\overline{D}_{i+1/2,j,k}=signA_{i+1/2,j,k}\left(I-\Delta t^{2}_{i,j,k}\left|A_{i+1/2,j,k}\right|^{2}\right)\Delta_{+}Q_{i,j,k}/6. \quad (80)$$

Observe that the resulting scheme is equivalent to the original of [24], with the unique difference that the difference of fluxes in Eqs. (72-73) is changed by the difference of conserved variables. With this new definition, the solutions present better behaviour, free of oscillations, undershoots and overshoots. The other expressions maintain the same structure.

The same equations, considered in η and ζ directions, can be developed, without any additional complexity. The algorithm described above is referred by [24] as TVD3 and the present authors remain this nomenclature.

The definition of the RHS to the implicit formulation is done as follows:

$$RHS(Y)^{n}_{i,j,k}=-\frac{\Delta t_{i,j,k}}{V_{i,j,k}}\left(E^{TVD3}_{i+1/2,j,k}-E^{TVD3}_{i-1/2,j,k}\right)-\frac{\Delta t_{i,j,k}}{V_{i,j,k}}\left(F^{TVD3}_{i,j+1/2,k}-F^{TVD3}_{i,j-1/2,k}\right)-\frac{\Delta t_{i,j,k}}{V_{i,j,k}}\left(G^{TVD3}_{i,j,k+1/2}-G^{TVD3}_{i,j,k-1/2}\right). \quad (81)$$

The Strang method is applied to the viscous simulations.

5.2 ENO formulation

A third-order ENO scheme for Eq. (68) can be constructed using reconstruction by primitive variable. Here, it is adopted:

$$E^{M}_{i,j,k}=E^{ENO3}_{i,j,k}=E^{n}_{i,j,k}+T^{n}_{i,j,k}+D^{n}_{i,j,k};$$
$$F^{M}_{i,j,k}=F^{ENO3}_{i,j,k}=F^{n}_{i,j,k}+U^{n}_{i,j,k}+D^{n}_{i,j,k};$$
$$G^{M}_{i,j,k}=G^{ENO3}_{i,j,k}=G^{n}_{i,j,k}+V^{n}_{i,j,k}+D^{n}_{i,j,k}, \quad (82)$$

and *T*, *U*, *V* and *D* are the terms that make up for the higher order accuracy that also depends either the TVD or the ENO property to avoid Gibbs phenomena.

In Eq. (82) the components of the column vector $T_{i,j,k}$ are given by

$$t^{l}_{i,j,k}=m\left(\tilde{t}^{l}_{i+1/2,j,k},\tilde{t}^{l}_{i-1/2,j,k}\right), \quad (83)$$

where $\tilde{t}^{l}_{i+1/2,j,k}$ is given by

$$\tilde{T}_{i+1/2,j,k}=signA_{i+1/2,j,k}\left(I-\Delta t_{i,j,k}\left|A_{i+1/2,j,k}\right|\right)\Delta_{+}E_{i,j,k}/2. \quad (84)$$

And the components of column vector $D_{i,j,k}$ are given by

$$d^{l}_{i,j,k}=m\left(\Delta_{-}\tilde{d}^{l}_{i-1/2,j,k},\Delta_{+}\tilde{d}^{l}_{i-1/2,j,k}\right) \quad if \quad \left|\Delta_{i-1/2,j,k}q^{l}\right|\le\left|\Delta_{i+1/2,j,k}q^{l}\right|;$$

or,

$$d^{l}_{i,j,k}=m\left(\Delta_{-}\hat{d}^{l}_{i+1/2,j,k},\Delta_{+}\hat{d}^{l}_{i+1/2,j,k}\right) \quad if \quad \left|\Delta_{i-1/2,j,k}q^{l}\right|>\left|\Delta_{i+1/2,j,k}q^{l}\right|, \quad (85)$$

where $\tilde{d}^{l}_{i+1/2,j,k}$ and $\hat{d}^{l}_{i-1/2,j,k}$ are components of $\tilde{D}_{i+1/2,j,k}$ and $\hat{D}_{i+1/2,j,k}$, respectively.

$\tilde{D}_{i+1/2,j,k}$ is given by Eq. (72) and $\hat{D}_{i+1/2,j,k}$ is given by

$$\hat{D}_{i+1/2,j,k} = signA_{i+1/2,j,k}\left(\Delta t_{i,j,k}^2\left|A_{i+1/2,j,k}\right|^2 - I\right)\Delta_+ E_{i,j,k}/6\ . \tag{86}$$

This author also introduces a modification in the original algorithm of [24] in its ENO3 (ENO third-order) version. This modification is the same as that applied to the TVD3 scheme. Hence,

$$\begin{aligned} E_{i,j,k}^M &= E_{i,j,k}^{ENO3} = E_{i,j,k}^n + A_{\xi_{i+1/2,j,k}} T_{i,j,k}^n + A_{\xi_{i+1/2,j,k}} D_{i,j,k}^n; \\ F_{i,j,k}^M &= F_{i,j,k}^{ENO3} = F_{i,j,k}^n + B_{\eta_{i,j+1/2,k}} U_{i,j,k}^n + B_{\eta_{i,j+1/2,k}} D_{i,j,k}^n; \\ G_{i,j,k}^M &= G_{i,j,k}^{ENO3} = G_{i,j,k}^n + C_{\eta_{i,j,k+1/2}} V_{i,j,k}^n + C_{\eta_{i,j,k+1/2}} D_{i,j,k}^n; \end{aligned} \tag{87}$$

$$\begin{aligned} \tilde{T}_{i+1/2,j,k} &= signA_{i+1/2,j,k}\left(I - \Delta t_{i,j,k}\left|A_{i+1/2,j,k}\right|\right)\Delta_+ Q_{i,j,k}/2; \\ \hat{D}_{i+1/2,j,k} &= signA_{i+1/2,j,k}\left(\Delta t_{i,j,k}^2\left|A_{i+1/2,j,k}\right|^2 - I\right)\Delta_+ Q_{i,j,k}/6 \end{aligned} \tag{88}$$

and $\tilde{D}_{i+1/2,j,k}$ defined as in Eq. (79). The other equations maintain the same aspect. The extension to the η and ζ directions is straightforward.

The definition of the RHS to the implicit formulation is done as follows:

$$RHS(Y)_{i,j,k}^n = -\frac{\Delta t_{i,j,k}}{V_{i,j,k}}\left(E_{i+1/2,j,k}^{ENO3} - E_{i-1/2,j,k}^{ENO3}\right) - \frac{\Delta t_{i,j,k}}{V_{i,j,k}}\left(F_{i,j+1/2,k}^{ENO3} - F_{i,j-1/2,k}^{ENO3}\right) + \frac{\Delta t_{i,j,k}}{V_{i,j,k}}\left(G_{i,j,k+1/2}^{ENO3} - G_{i,j,k-1/2}^{ENO3}\right). \tag{89}$$

The Strang method is applied to the viscous simulations.

6 Yang and Hsu UNO Third Order Algorithm

Unlike TVD schemes, nonoscillatory algorithms are not required to damp the values of each local extremum at every single time step, but are allowed to occasionally accentuate a local extremum. The design involves an essentially nonoscillatory piecewise polynomial reconstruction of the solution from its cell averages, time evolution through an approximate solution of the resulting initial value problem, and averaging of this approximate solution over each cell.

A third-order UNO scheme for Eq. (1), based on [25] work, can be expressed by the following numerical flux, in ξ direction, for instance:

$$E_{i+1/2,j,k}^{UNO3} = \frac{1}{2}\left(E_{i,j,k}^n + E_{i+1,j,k}^n + R_{i+1/2,j,k}^{\xi,n}\Phi_{i+1/2,j,k}^{UNO3}\right). \tag{90}$$

The components of $\Phi_{i+1/2,j,k}^{UNO3}$ are defined as:

$$\begin{aligned} \phi_{i+1/2,j,k}^{l,UNO3} &= \sigma\left(\lambda_{i+1/2,j,k}^l\right)\left(\beta_{i,j,k}^l + \beta_{i+1,j,k}^l\right) \\ &+ \begin{cases} \tilde{\sigma}\left(\lambda_{i+1/2,j,k}^n\right)\left(\tilde{\beta}_{i,j,k}^l + \tilde{\beta}_{i+1,j,k}^l\right) - \psi\left(\lambda_{i+1/2,j,k}^l + \gamma_{i+1/2,j,k}^l + \tilde{\gamma}_{i+1/2,j,k}^l\right)\alpha_{i+1/2,j,k}^l \\ \qquad if\ \left|\alpha_{i-1/2,j,k}^l\right| \le \left|\alpha_{i+1/2,j,k}^l\right| \\ \hat{\sigma}\left(\lambda_{i+1/2,j,k}^n\right)\left(\hat{\beta}_{i,j,k}^l + \hat{\beta}_{i+1,j,k}^l\right) - \psi\left(\lambda_{i+1/2,j,k}^l + \gamma_{i+1/2,j,k}^l + \hat{\gamma}_{i+1/2,j,k}^l\right)\alpha_{i+1/2,j,k}^l \\ \qquad otherwise \end{cases}, \end{aligned} \tag{91}$$

where the σ, $\tilde{\sigma}$ and $\hat{\sigma}$ functions are given by:

$$\sigma = \frac{1}{2}\left[\psi(z) - \Delta t_{i,j,k} z^2\right]; \tag{92}$$

$$\tilde{\sigma} = \frac{1}{6}\left[2|z| - 3\Delta t_{i,j,k}|z|^2 + \Delta t_{i,j,k}^2|z|^3\right]; \tag{93}$$

$$\hat{\sigma} = \frac{1}{6}\left[\Delta t_{i,j,k}^2|z|^3 - |z|\right], \tag{94}$$

and

$$\beta_{i,j,k}^l = m\left(\alpha_{i+1/2,j,k}^l, \alpha_{i-1/2,j,k}^l\right); \tag{95}$$

$$\tilde{\beta}_{i,j,k}^l = \overline{m}\left(\Delta_-\alpha_{i-1/2,j,k}^l, \Delta_+\alpha_{i-1/2,j,k}^l\right)\ \ if\ \ \left|\alpha_{i-1/2,j,k}^l\right| \le \left|\alpha_{i+1/2,j,k}^l\right|; \tag{96}$$

$$\hat{\beta}_{i,j,k}^l = \overline{m}\left(\Delta_-\alpha_{i+1/2,j,k}^l, \Delta_+\alpha_{i+1/2,j,k}^l\right)\ \ if\ \ \left|\alpha_{i-1/2,j,k}^l\right| > \left|\alpha_{i+1/2,j,k}^l\right|; \tag{97}$$

$$\gamma_{i+1/2,j,k}^l = \sigma\left(\lambda_{i+1/2,j,k}^l\right)\begin{cases}\left(\beta_{i+1,j,k}^l - \beta_{i,j,k}^l\right)/\alpha_{i+1/2,j,k}^l & if\ \ \alpha_{i+1/2,j,k}^l \ne 0 \\ 0, & otherwise\end{cases}; \tag{98}$$

$$\tilde{\gamma}_{i+1/2,j,k}^l = \tilde{\sigma}\left(\lambda_{i+1/2,j,k}^l\right)\begin{cases}\left(\tilde{\beta}_{i+1,j,k}^l - \tilde{\beta}_{i,j,k}^l\right)/\alpha_{i+1/2,j,k}^l & if\ \ \alpha_{i+1/2,j,k}^l \ne 0 \\ 0, & otherwise\end{cases}; \tag{99}$$

$$\hat{\gamma}_{i+1/2,j,k}^l = \hat{\sigma}\left(\lambda_{i+1/2,j,k}^l\right)\begin{cases}\left(\hat{\beta}_{i+1,j,k}^l - \hat{\beta}_{i,j,k}^l\right)/\alpha_{i+1/2,j,k}^l & if\ \ \alpha_{i+1/2,j,k}^l \ne 0 \\ 0, & otherwise\end{cases}. \tag{100}$$

The same expressions can be extended to the η and ζ directions in a straightforward way. To the inviscid implicit cases, the LNI form is applied. The RHS for this algorithm is given by:

$$RHS\,(YH)^n_{i,j,k} = -\frac{\Delta t_{i,j,k}}{V_{i,j,k}}\left(E^{UNO3}_{i+1/2,j,k} - E^{UNO3}_{i-1/2,j,k}\right) - \frac{\Delta t_{i,j,k}}{V_{i,j,k}}\left(F^{UNO3}_{i,j+1/2,k} - F^{UNO3}_{i,j-1/2,k}\right) - \frac{\Delta t_{i,j,k}}{V_{i,j,k}}\left(G^{UNO3}_{i,j,k+1/2} - G^{UNO3}_{i,j,k-1/2}\right). \quad (101)$$

To the explicit viscous case, the Strang method is applied:

$$Q^{n+2}_{i,j,k} = L_\xi(\Delta t)L_\eta(\Delta t)L_\zeta(\Delta t)L_\zeta(\Delta t)L_\eta(\Delta t)L_\xi(\Delta t)Q^n_{i,j,k}\,. \quad (102)$$

The L_ξ operator is defined by

$$L_\xi(\Delta t)Q^n_{i,j,k} = Q^n_{i,j,k} - \Delta t\left(E^{UNO}_{i+1/2,j,k} - E^{UNO}_{i-1/2,j,k}\right). \quad (103)$$

7 Implicit Formulation

7.1 Implicit Scheme to the TVD algorithm of [12] and the UNO algorithm of [25]

In the flux difference splitting cases of [12; 25] algorithms, a Linearized Nonconservative Implicit form is applied which, although the resulting schemes lose the conservative property, they preserve their unconditional TVD properties. Moreover, the LNI form is mainly useful to steady state problems where the conservative property is recovery by these schemes in such condition. This LNI form was proposed by [11].

The LNI form is defined by the following three step algorithm:

$$\left[I - \Delta t_{i,j,k}J^-_{i+1/2,j,k}\Delta_{i+1/2,j,k} + \Delta t_{i,j,k}J^+_{i-1/2,j,k}\Delta_{i-1/2,j,k}\right]\Delta Q^*_{i,j,k} = [RHS]^n_{i,j,k}\,, \text{ in the } \xi \text{ direction;} \quad (104)$$

$$\left[I - \Delta t_{i,j,k}K^-_{i,j+1/2,k}\Delta_{i,j+1/2,k} + \Delta t_{i,j,k}K^+_{i,j-1/2,k}\Delta_{i,j-1/2,k}\right]\Delta Q^{**}_{i,j,k} = \Delta Q^*_{i,j,k}\,, \text{ in the } \eta \text{ direction;} \quad (105)$$

$$\left[I - \Delta t_{i,j,k}L^-_{i,j,k+1/2}\Delta_{i,j,k+1/2} + \Delta t_{i,j,k}L^+_{i,j,k-1/2}\Delta_{i,j,k-1/2}\right]\Delta Q^{n+1}_{i,j,k} = \Delta Q^{**}_{i,j,k}\,, \text{ in the } \zeta \text{ direction;} \quad (105)$$

$$Q^{n+1}_{i,j,k} = Q^n_{i,j,k} + \Delta Q^{n+1}_{i,j,k}\,, \quad (106)$$

where RHS is defined by Eq. (40), if the [12] scheme is being solved, and by Eq. (101), if the [25] scheme is being solved. The difference operators are defined as:

$$\Delta_{i+1/2,j,k}(\cdot) = (\cdot)_{i+1,j,k} - (\cdot)_{i,j,k},\ \Delta_{i-1/2,j,k}(\cdot) = (\cdot)_{i,j,k} - (\cdot)_{i-1,j,k}; \quad (107)$$

$$\Delta_{i,j+1/2,k}(\cdot) = (\cdot)_{i,j+1,k} - (\cdot)_{i,j,k},\ \Delta_{i,j-1/2,k}(\cdot) = (\cdot)_{i,j,k} - (\cdot)_{i,j-1,k}; \quad (108)$$

$$\Delta_{i,j,k+1/2}(\cdot) = (\cdot)_{i,j,k+1} - (\cdot)_{i,j,k},\ \Delta_{i,j,k-1/2}(\cdot) = (\cdot)_{i,j,k} - (\cdot)_{i,j,k-1}; \quad (109)$$

As aforementioned, this three-diagonal linear system, composed of a 5x5 block matrices, is solved using LU decomposition and the Thomas algorithm, defined by a block matrix system.

The separated matrices J^+, J^-, K^+, K^-, L^+ and L^- are defined as follows:

$$J^+ = R_\xi\,diag\left(D^+_\xi\right)R^{-1}_\xi,\ J^- = R_\xi\,diag\left(D^-_\xi\right)R^{-1}_\xi \quad (110)$$

$$K^+ = R_\eta\,diag\left(D^+_\eta\right)R^{-1}_\eta,\ K^- = R_\eta\,diag\left(D^-_\eta\right)R^{-1}_\eta \quad (111)$$

$$L^+ = R_\zeta\,diag\left(D^+_\zeta\right)R^{-1}_\zeta,\ L^- = R_\zeta\,diag\left(D^-_\zeta\right)R^{-1}_\zeta\,. \quad (112)$$

The diagonal matrices of the [12; 25] schemes are determined by:

$$diag\left(D^+_\xi\right) = \begin{bmatrix} D^{\xi,+}_1 & & & & \\ & D^{\xi,+}_2 & & & \\ & & D^{\xi,+}_3 & & \\ & & & D^{\xi,+}_4 & \\ & & & & D^{\xi,+}_5 \end{bmatrix} \text{ and}$$

$$diag\left(D^-_\xi\right) = \begin{bmatrix} D^{\xi,-}_1 & & & & \\ & D^{\xi,-}_2 & & & \\ & & D^{\xi,-}_3 & & \\ & & & D^{\xi,-}_4 & \\ & & & & D^{\xi,-}_5 \end{bmatrix} \quad (113)$$

with the D terms expressed as

$$D^\pm_\xi = 0.5\left[\Psi\left(\lambda^l_\xi + \gamma^l_\xi\right) \pm \left(\lambda^l_\xi + \gamma^l_\xi\right)\right],$$
$$D^\pm_\eta = 0.5\left[\Psi\left(\lambda^l_\eta + \gamma^l_\eta\right) \pm \left(\lambda^l_\eta + \gamma^l_\eta\right)\right],$$
$$D^\pm_\zeta = 0.5\left[\Psi\left(\lambda^l_\zeta + \gamma^l_\zeta\right) \pm \left(\lambda^l_\zeta + \gamma^l_\zeta\right)\right], \quad (114)$$

where:

Ψ defined by Eq. (32);

λ^l_ξ, λ^l_η and λ^l_ζ are the eigenvalues of the Euler equations, determined by Eqs. (25-26), in each coordinate direction;

$$\left(\gamma^l_\xi\right)_{i+1/2,j,k} = \begin{cases} \left[\left(g'_\xi\right)^l_{i+1,j,k} - \left(g'_\xi\right)^l_{i,j,k}\right] \Big/ \left(\alpha^l_\xi\right)_{i+1/2,j,k}, & if\ \left(\alpha^l_\xi\right)_{i+1/2,j,k} \neq 0.0 \\ 0.0, & if\ \left(\alpha^l_\xi\right)_{i+1/2,j,k} = 0.0 \end{cases}; \quad (115)$$

$$\left(\gamma_{\eta}^{l}\right)_{i,j+1/2,k}=\begin{cases}\left[\left(g_{\eta}^{'}\right)_{i,j+1,k}^{l}-\left(g_{\eta}^{'}\right)_{i,j,k}^{l}\right]/\left(\alpha_{\eta}^{l}\right)_{i,j+1/2,k}, & if\left(\alpha_{\eta}^{l}\right)_{i,j+1/2,k}\neq 0.0\\ 0.0, & if\left(\alpha_{\eta}^{l}\right)_{i,j+1/2,k}=0.0\end{cases}; \quad (116)$$

$$\left(\gamma_{\zeta}^{l}\right)_{i,j+1/2,k}=\begin{cases}\left[\left(g_{\zeta}^{'}\right)_{i,j,k+1}^{l}-\left(g_{\zeta}^{'}\right)_{i,j,k}^{l}\right]/\left(\alpha_{\zeta}^{l}\right)_{i,j,k+1/2}, & if\left(\alpha_{\zeta}^{l}\right)_{i,j,k+1/2}\neq 0.0\\ 0.0, & if\left(\alpha_{\zeta}^{l}\right)_{i,j,k+1/2}=0.0\end{cases}; \quad (117)$$

$$\left(g_{\xi}^{'}\right)_{i,j,k}^{l}=signal_{\xi}^{l}MAX\left[0.0,MIN\left(\sigma_{i+1/2,j,k}^{l}\left|\left(\alpha_{\xi}^{l}\right)_{i+1/2,j,k}\right|,signal_{\xi}^{l}\sigma_{i-1/2,j,k}^{l}\left(\alpha_{\xi}^{l}\right)_{i-1/2,j,k}\right)\right]; \quad (118)$$

$$\left(g_{\eta}^{'}\right)_{i,j,k}^{l}=signal_{\eta}^{l}MAX\left[0.0,MIN\left(\sigma_{i,j+1/2,k}^{l}\left|\left(\alpha_{\eta}^{l}\right)_{i,j+1/2,k}\right|,signal_{\eta}^{l}\sigma_{i,j-1/2,k}^{l}\left(\alpha_{\eta}^{l}\right)_{i,j-1/2,k}\right)\right]; \quad (119)$$

$$\left(g_{\zeta}^{'}\right)_{i,j,k}^{l}=signal_{\zeta}^{l}MAX\left[0.0,MIN\left(\sigma_{i,j,k+1/2}^{l}\left|\left(\alpha_{\zeta}^{l}\right)_{i,j,k+1/2}\right|,signal_{\zeta}^{l}\sigma_{i,j,k-1/2}^{l}\left(\alpha_{\zeta}^{l}\right)_{i,j,k-1/2}\right)\right]; \quad (120)$$

$$\sigma^{1}=1/2\,\Psi^{1}\left(\lambda^{1}\right) \text{ to steady state simulations.} \quad (121)$$

Finally, $signal_{\xi}^{l}$ = 1.0 if $\left(\alpha_{\xi}^{l}\right)_{i+1/2,j,k}\geq 0.0$ and -1.0 otherwise; $signal_{\eta}^{l}$ = 1.0 if $\left(\alpha_{\eta}^{l}\right)_{i,j+1/2,k}\geq 0.0$ and -1.0 otherwise; $signal_{\zeta}^{l}$ = 1.0 if $\left(\alpha_{\zeta}^{l}\right)_{i,j,k+1/2}\geq 0.0$ and -1.0 otherwise.

This implicit formulation to the LHS of the TVD or UNO schemes of [12] and [25], respectively, is second order accurate in space and first order accurate in time due to the presence of the characteristic numerical speed γ associated with the numerical flux function g'. In this case, the algorithms accuracy is definitely second order in space because both LHS and RHS are second order accurate.

7.2 Implicit Scheme to the TVD/ENO algorithms of [21; 24]

For these algorithms, a backward Euler method in time and approximate factorization ADI form can be employed. The factorization in each coordinate direction is presented below:

$$\left[I+\Delta t_{i,j,k}\hat{A}_{i-1/2,j,k}^{+}\Delta_{-}A_{\xi}+\Delta t_{i,j,k}\hat{A}_{i+1/2,j,k}^{-}\Delta_{+}A_{\xi}\right]\Delta Q_{i,j,k}^{*}=RHS_{i,j,k}^{n}; \quad (122)$$

$$\left[I+\Delta t_{i,j,k}\hat{B}_{i,j-1/2,k}^{+}\Delta_{-}B_{\eta}+\Delta t_{i,j,k}\hat{B}_{i,j+1/2,k}^{-}\Delta_{+}B_{\eta}\right]\Delta Q_{i,j,k}^{**}=\Delta Q_{i,j,k}^{*}; \quad (123)$$

$$\left[I+\Delta t_{i,j,k}\hat{C}_{i,j,k-1/2}^{+}\Delta_{-}C_{\zeta}+\Delta t_{i,j,k}\hat{C}_{i,j,k+1/2}^{-}\Delta_{+}C_{\zeta}\right]\Delta Q_{i,j,k}^{n+1}=\Delta Q_{i,j,k}^{**}; \quad (124)$$

$$Q_{i,j,k}^{n+1}=Q_{i,j,k}^{n}+\Delta Q_{i,j,k}^{n+1}. \quad (125)$$

Equations (122-124) lead to standard block three-diagonal inversion procedure. The Thomas algorithm is employed to solve this system.

The matrices above are all defined along this manuscript, being unnecessary repeat them herein.

It is noted that each added high-order term of the right-hand-side operator [Eqs. (65; 81; 89)] is a function of the time step $\Delta t_{i,j,k}$, and consequently the steady state solutions will depend on the time step.

It is important to emphasize that the RHS of the flux difference splitting implicit schemes present steady state solutions which depend of the time step. With this behavior, the use of large time steps can affect the stationary solutions, as mentioned in [40]. This is an initial study with implicit schemes and improvements in the numerical implementation of these algorithms with steady state solutions independent of the time step is a goal to be reached in future work of this author.

8 Spatially Variable Time Step

The basic idea of this procedure consists in keeping constant the CFL number in all calculation domain, allowing, hence, the use of appropriated time steps to each specific mesh region during the convergence process. According to the definition of the CFL number, it is possible to write:

$$\Delta t_{i,j,k}=CFL\left(\Delta s\right)_{i,j,k}/c_{i,j,k}, \quad (126)$$

where CFL is the "Courant-Friedrichs-Lewy" number to provide numerical stability to the scheme; $c_{i,j,k}=\left[\left(u^{2}+v^{2}+w^{2}\right)^{0.5}+a\right]_{i,j,k}$ is the maximum characteristic speed of information propagation in the calculation domain; and $\left(\Delta s\right)_{i,j,k}$ is a characteristic length of information transport. On a finite volume context, $\left(\Delta s\right)_{i,j,k}$ is chosen as the minor value found between the minor barycenter distance, involving the *(i,j,k)* cell and a neighbor, and the minor cell side length.

9 Initial and Boundary Conditions

9.1 Initial Condition

To the physical problems studied in this work, freestream flow values are adopted for all properties as initial condition, in the whole calculation domain ([41-42]). Therefore, the vector of conserved variables is defined as:

$$Q_{i,j} = \left\{ 1 \quad M_\infty \cos\alpha \quad M_\infty \sin\alpha \quad \frac{1}{\gamma(\gamma-1)} + 0.5M_\infty^2 \right\}^T, \tag{127}$$

being α the flow attack angle.

9.2 Boundary Conditions

The boundary conditions are basically of three types: solid wall, entrance and exit. The far field condition is a case of entrance and exit frontiers. These conditions are implemented in special cells named ghost cells.

(a) Wall condition: This condition imposes the flow tangency at the solid wall. This condition is satisfied considering the wall tangent velocity component of the ghost volume as equals to the respective velocity component of its real neighbor cell. At the same way, the wall normal velocity component of the ghost cell is equaled in value, but with opposite signal, to the respective velocity component of the real neighbor cell. According to [43], it results in:

$$u_g = (1-2n_x n_x)u_{real} + (-2n_x n_y)v_{real} + (-2n_x n_z)w_{real}; \tag{128}$$

$$v_g = (-2n_y n_x)u_{real} + (1-2n_y n_y)v_{real} + (-2n_y n_z)w_{real}; \tag{129}$$

$$w_g = (-2n_z n_x)u_{real} + (-2n_z n_y)v_{real} + (1-2n_z n_z)w_{real}, \tag{130}$$

with "g" related with ghost cell and "r" related with real cell. To the viscous case, the boundary condition imposes that the ghost cell velocity components be equal to the real cell velocity components, with the negative signal:

$$u_g = -u_{real}; \tag{131}$$

$$v_g = -v_{real}, \tag{132}$$

$$w_g = -w_{real}. \tag{133}$$

The pressure gradient normal to the wall is assumed be equal to zero, following an inviscid formulation and according to the boundary layer theory. The same hypothesis is applied to the temperature gradient normal to the wall, considering adiabatic wall. The ghost volume density and pressure are extrapolated from the respective values of the real neighbor volume (zero order extrapolation), with these two conditions. The total energy is obtained by the state equation of a perfect gas.

(b) Entrance condition:
(b.1) Subsonic flow: Four properties are specified and one is extrapolated, based on analysis of information propagation along characteristic directions in the calculation domain ([42]). In other words, four characteristic directions of information propagation point inward the computational domain and should be specified. Only the characteristic direction associated to the "*(q_n-a)*" velocity cannot be specified and should be determined by interior information of the calculation domain. The pressure was the extrapolated variable from the real neighbor volume, to the studied problems. Density and velocity components had their values determined by the freestream flow properties. The total energy per unity fluid volume is determined by the state equation of a perfect gas.
(b.2) Supersonic flow: All variables are fixed with their freestream flow values.

(c) Exit condition:
(c.1) Subsonic flow: Four characteristic directions of information propagation point outward the computational domain and should be extrapolated from interior information ([42]). The characteristic direction associated to the "*(q_n-a)*" velocity should be specified because it penetrates the calculation domain. In this case, the ghost volume's pressure is specified by its freestream value. Density and velocity components are extrapolated and the total energy is obtained by the state equation of a perfect gas.
(c.2) Supersonic flow: All variables are extrapolated from the interior domain due to the fact that all five characteristic directions of information propagation of the Euler equations point outward the calculation domain and, with it, nothing can be fixed.

10 Results

Tests were performed in a personal computer (notebook) with Pentium dual core processor of 2.20GHz of clock and 2.0Gbytes of RAM memory. Converged results occurred to 3 orders of reduction in the value of the maximum residual. The maximum residual is defined as the maximum value obtained from the discretized conservation equations. To all problems, the attack angle was adopted equal to 0.0°.

The physical problems to be studied are the supersonic flows along a compression corner and along a ramp, in the inviscid case, and the supersonic flow also along a ramp, in the viscous case.

10.1 Ramp Problem - Inviscid

The ramp configuration is described in Fig. 1. The ramp inclination angle is 20°. An algebraic mesh of

61x60x10 points or composed of 31,860 hexahedrons and 36,600 nodes was used as shown in Fig. 2. The points are equally spaced in both directions.

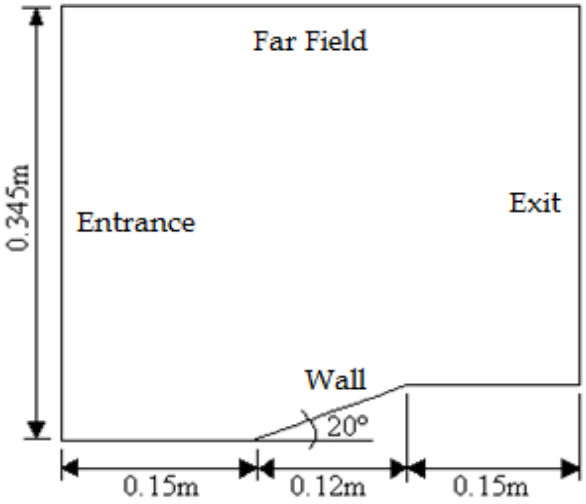

Figure 1. Ramp configuration.

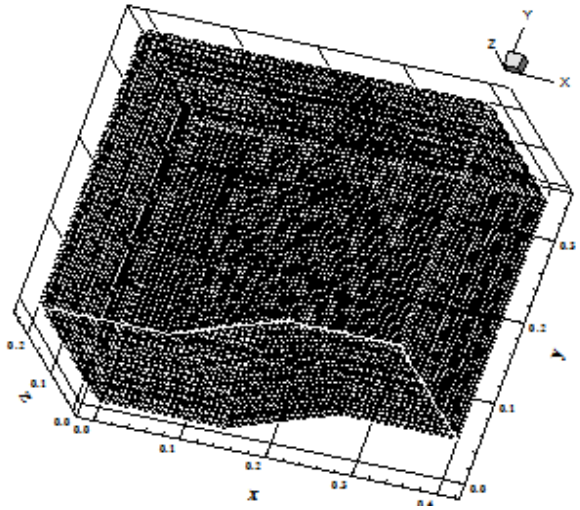

Figure 2. Ramp mesh (61x60x10).

This problem consists in a low supersonic flow impinging a ramp, where an oblique shock wave and an expansion fan are generated. The freestream Mach number is equal to 2.0. The solutions are compared with the oblique shock wave theory and the Prandtl-Meyer expansion fan theory.

In the figures below is employed the following nomenclature to the algorithms: TVD2 (Total Variation Diminishing, second order accurate in space), ENO2 (Essentially Nonocillatory, second order accurate in space), TVD3 (Total Variation Diminishing, third order accurate in space), ENO3 (Essencially Nonoscillatory, third order accurate in space) and UNO3 (Uniformly Nonoscillatory, third order accurate in space).

10.1.1 Yee and Harten's results

Figure 3 shows the pressure contours generated by the [12] scheme. It is clear the pressure oscillation at the beginning of the ramp, which will originate a pressure peak in the wall pressure plot.

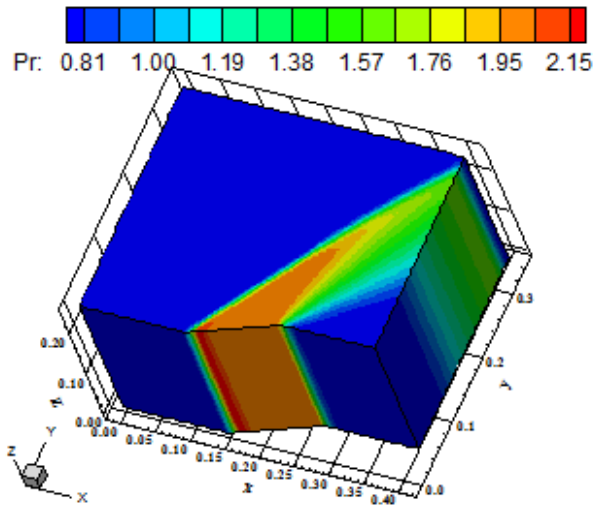

Figure 3. Pressure contours ([12]-TVD2).

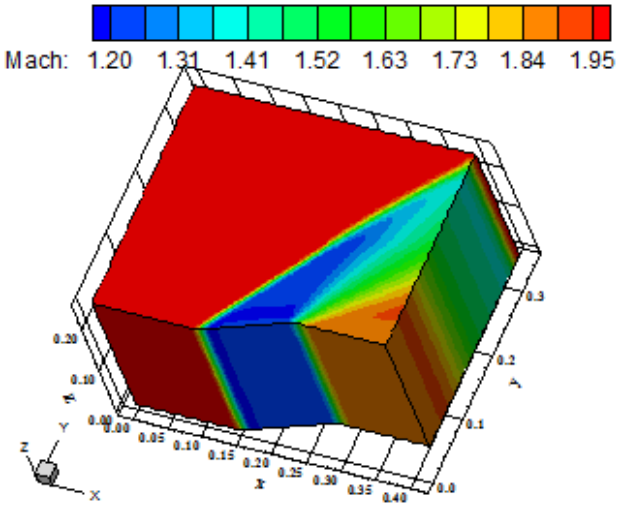

Figure 4. Mach number contours ([12]-TVD2).

Figure 4 exhibits the Mach number contours generated by [12] algorithm. The solution presents some overshoots at the ramp beginning. The homogeneity of the contours is clear, which guarantees the same solution at each k plane.

Figure 5 presents the wall pressure distribution generated by the [12] scheme. As can see, a pressure peak is captured by the algorithm at the discontinuity, which represents an unphysical behavior. Even so, the shock is captured in four (4) cells, which is a good result.

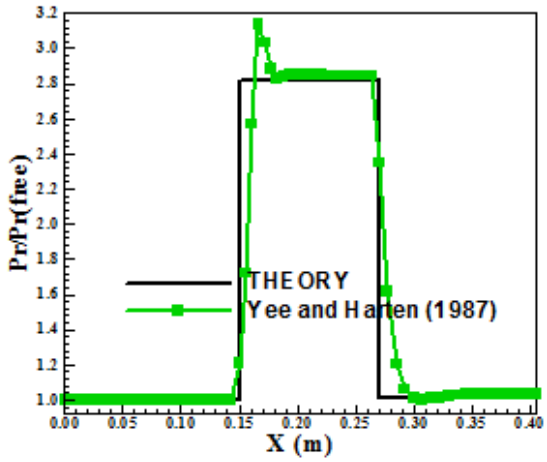

Figure 5. Wall pressure distribution ([12]).

10.1.2 Yang's second order results

Figures (6-7) show the pressure contours obtained by the TVD and ENO versions, respectively, of scheme [21]. It is possible to note that no overshoots or undershoots are presented. Moreover, the solutions in the k's planes are equal and this aspect of the 3D flow is assured. Figures (8-9) exhibit the Mach number contours generated by the TVD and ENO versions of [21]. The solutions are clear, without oscillations.

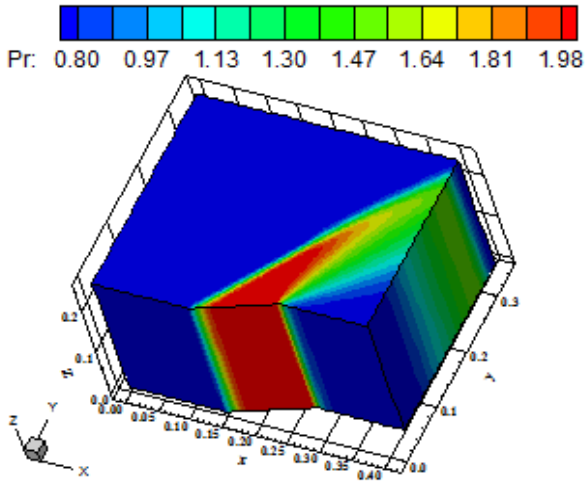

Figure 6. Pressure contours ([21]-TVD2).

Figure 10 presents the wall pressure distributions obtained by the [21] scheme. Both versions, TVD and ENO, capture the shock discontinuity in eight (8) cells, which is an excessive number of cells to a high resolution scheme capture a discontinuity. The excessive dissipation generated by the scheme, in its two versions, is responsible to this number of cells.

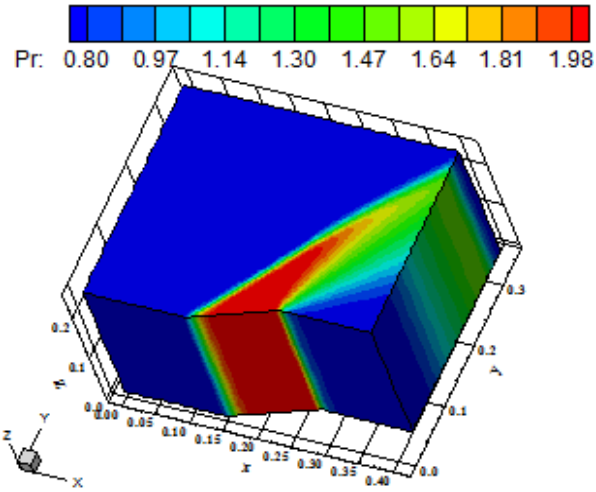

Figure 7. Pressure contours ([21-ENO2).

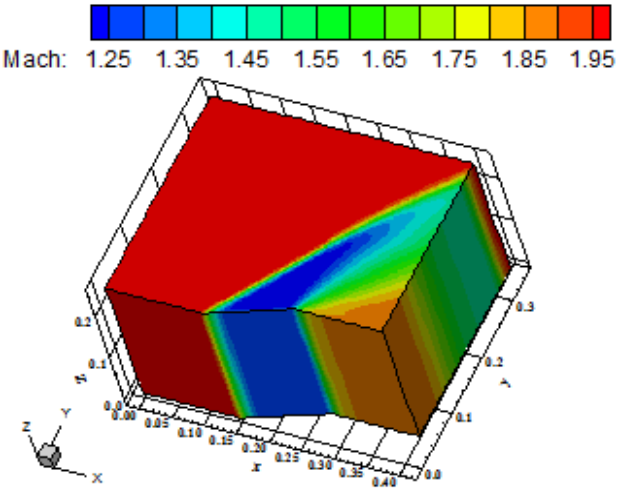

Figure 8. Mach number contours ([21]-TVD2).

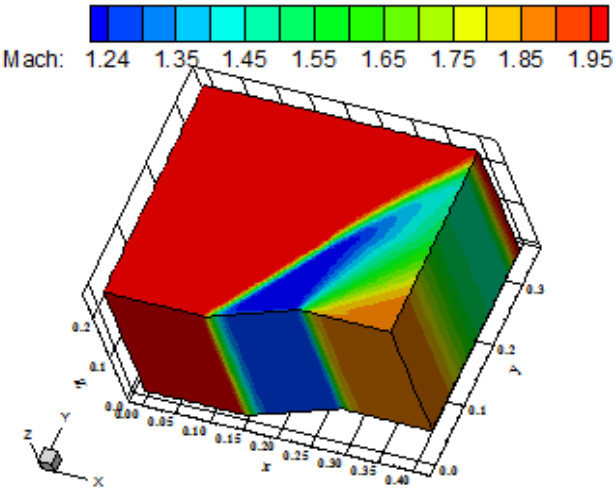

Figure 9. Mach number contours ([21]-ENO2).

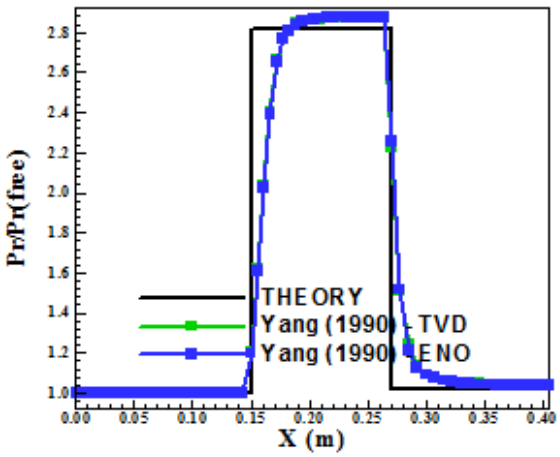

Figure 10. Wall pressure distributions ([21]).

10.1.3 Yang's third order results

Figures (11-12) present the pressure contours generated by the [24] scheme in its two versions, TVD and ENO, of third order spatial accuracy.

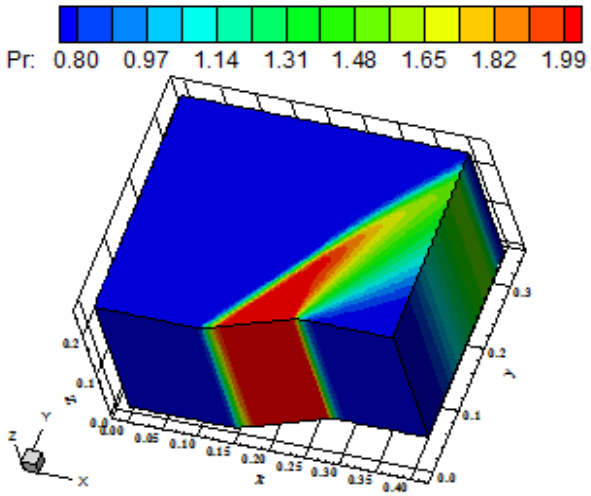

Figure 11. Pressure contours ([24]-TVD3).

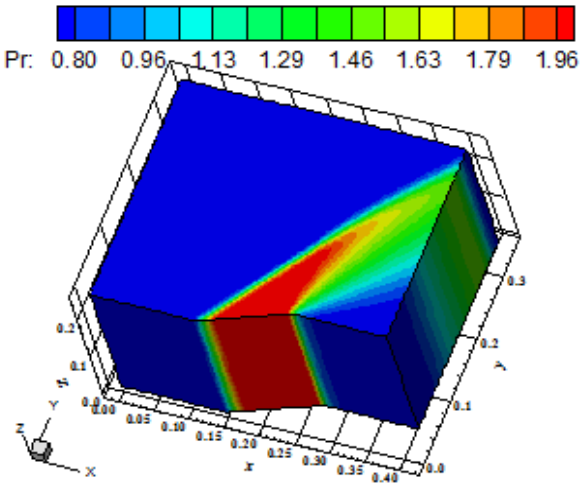

Figure 12. Pressure contours ([24]-ENO3).

Both solutions are clear, without oscillations. The 2D solution at each k plane is obtained, assuring the 3D behavior of reproducing such behavior.

Figures (13-14) show the Mach number contours generated by the [24] scheme in its two versions, TVD3 and ENO3. The shock is captured by both versions of scheme [24]. The smoothest solution is obtained by the ENO3 version of [24]. It is not observed overshoots or undershoots and the solution is clear and free of oscillations. The expansion fan region is also better detected by the ENO3 version of the [24] algorithm.

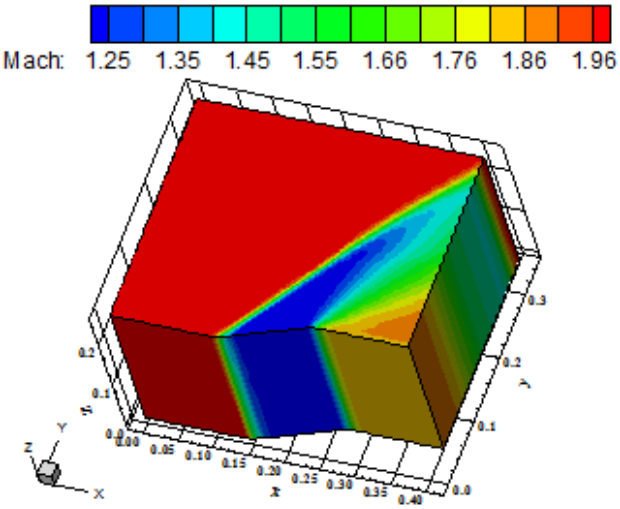

Figure 13. Mach number contours ([24]-TVD3).

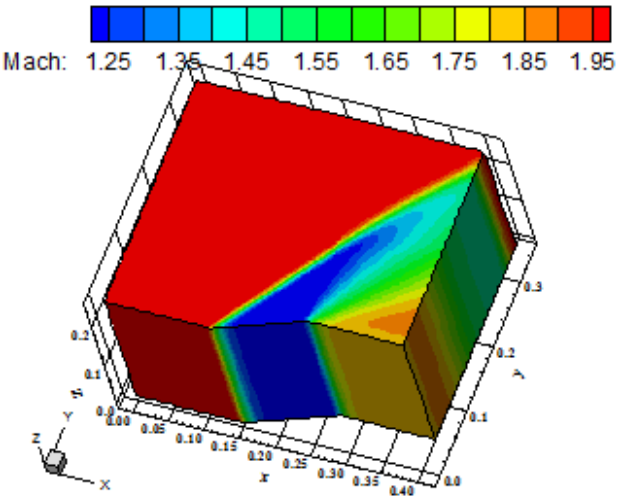

Figure 14. Mach number contours ([24]-ENO3).

Figure 15 exhibits the wall pressure distributions generated by scheme [24], in its two versions. As can see, both solutions present small differences. The TVD3 solution is closer to the shock profile, but presents an oscillation at the ramp ending. The ENO3 solution did not present such oscillation and is the best choice to this scheme. Both solutions

capture the shock discontinuity using five (5) cells, which is far better than the [21] solutions (TVD and ENO).

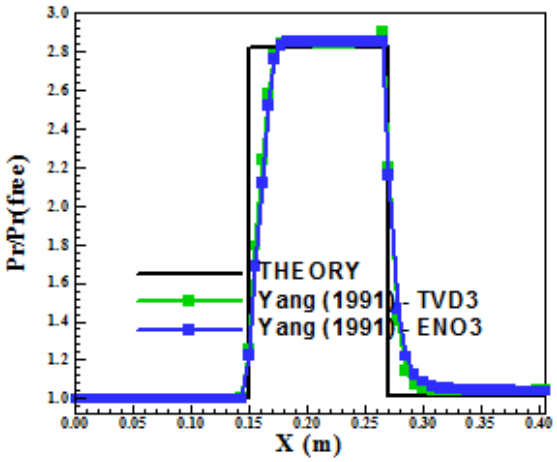

Figure 15. Wall pressure distributions ([24]).

10.1.4 Yang and Hsu's third order results

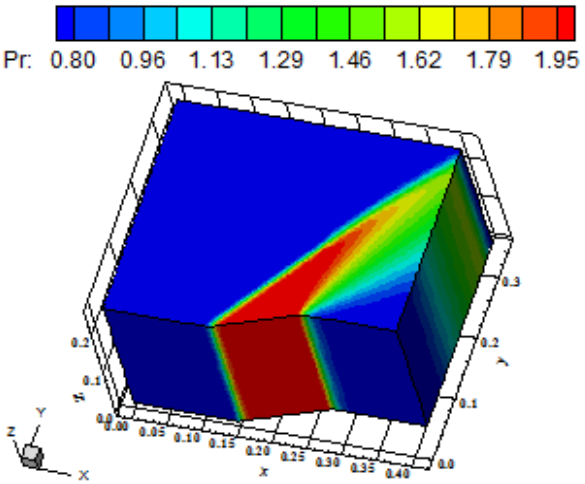

Figure 16. Pressure contours ([25]).

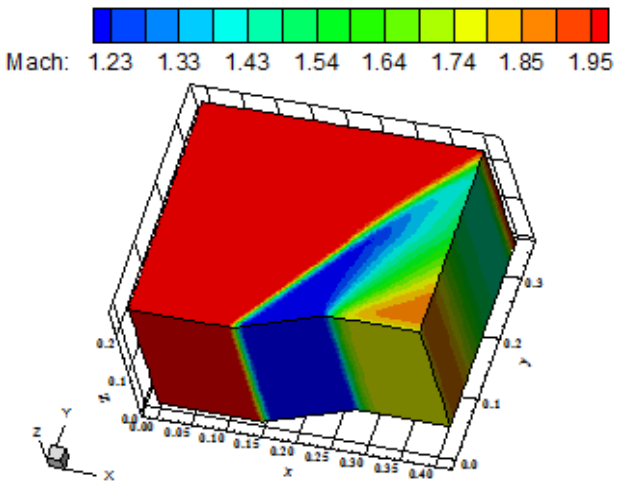

Figure 17. Mach number contours ([25]).

Figure 16 exhibits the pressure contours obtained by the [25] scheme. A clear solution is obtained with [25] algorithm. No oscillations are observed in this figure. Figure 17 shows the Mach number contours obtained by [25] scheme. A clear solution is also generated in terms of Mach number contours.

Figure 18 presents the wall pressure distribution generated by the [25] scheme. A better behavior in comparison with the other schemes is obtained by the [25] UNO3 scheme. The discontinuity is captured using four (4) cells.

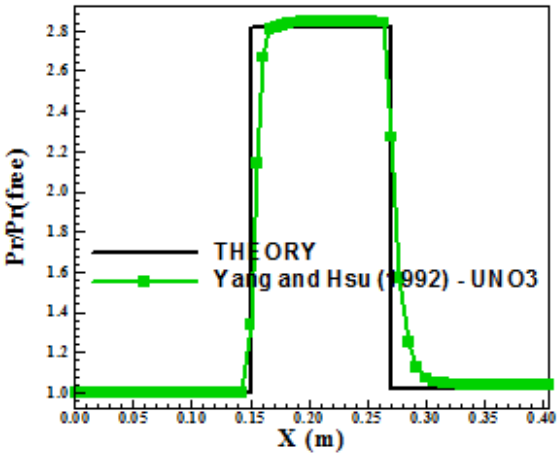

Figure 18. Wall pressure distribution ([25]).

By inspection with the other pressure distributions, it is evident that this wall pressure distribution generated by the [25] scheme is the best.

One way to quantitatively verify if the solutions generated by each scheme are satisfactory consists in determining the shock angle of the oblique shock wave, β, measured in relation to the initial direction of the flow field. [44] (pages 352 and 353) presents a diagram with values of the shock angle, β, to oblique shock waves. The value of this angle is determined as function of the freestream Mach number and of the deflection angle of the flow after the shock wave, ϕ.

Table 1. Shock angle and percentage errors.

Algotithm	β (°)	Error (%)
[12] – TVD2	53.0	0.00
[21] – TVD2	54.0	1.89
[21] – ENO2	53.0	0.00
[24] – TVD3	53.8	1.51
[24] – ENO3	53.0	0.00
[25] – UNO3	53.0	0.00

To the ramp problem, ϕ = 20º (ramp inclination angle) and the freestream Mach number is 2.0,

resulting from this diagram a value to β equals to 53.0º. Using a transfer in the pressure contours figures, at the xy plane, it is possible to obtain the values of β to each scheme, as well the respective errors, shown in Tab. 1. As can be observed, the [12] TVD2, the [21] ENO2, [24] ENO3 and [25] UNO3 algorithm has yielded the best results. Errors less than 2.0% were observed in all solutions.

10.2 Compression Corner Problem - Inviscid

The compression corner configuration is described in Fig. 19. The corner inclination angle is 10º. An algebraic mesh of 70x50x10 points or composed of 30,429 hexahedral cells and 35,000 nodes was used and is shown in Fig. 20. The points are equally spaced in both directions.

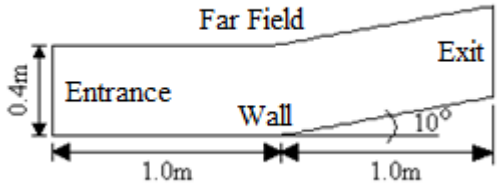

Figure 19. Compression corner configuration.

This problem consists in a moderate supersonic flow impinging a compression corner, where an oblique shock wave is generated. The freestream Mach number is equal to 3.0. The solutions are compared with the oblique shock wave theory results.

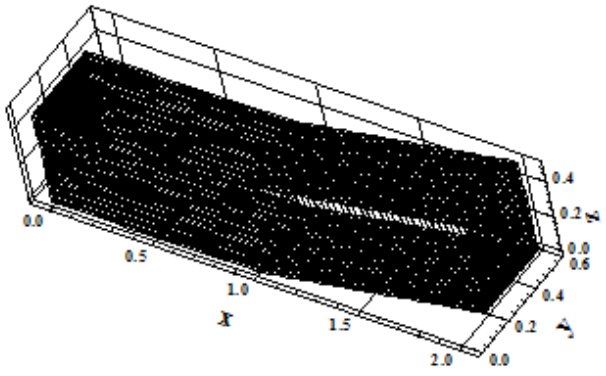

Figure 20. Compression corner mesh (70x50x10).

10.2.1 Yee and Harten's results

Figure 21 exhibits the pressure contours obtained by the [12] TVD2 scheme. As can be seen, a pressure peak appears at the corner beginning and it is reflected in the value 1.48 of the pressure legend, higher than the other solutions. Due to this behavior in the pressure contours, the wall pressure distribution of [12] presents this peak.

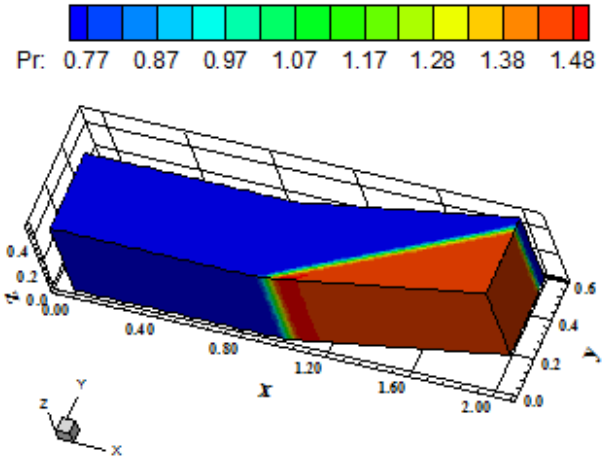

Figure 21. Pressure contours ([12]-TVD2).

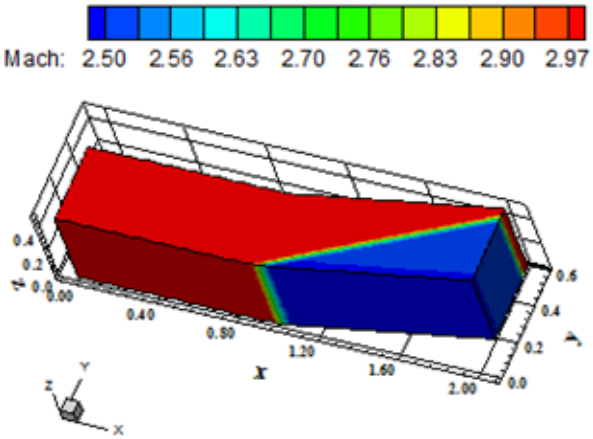

Figure 22. Mach number contours ([12]-TVD2).

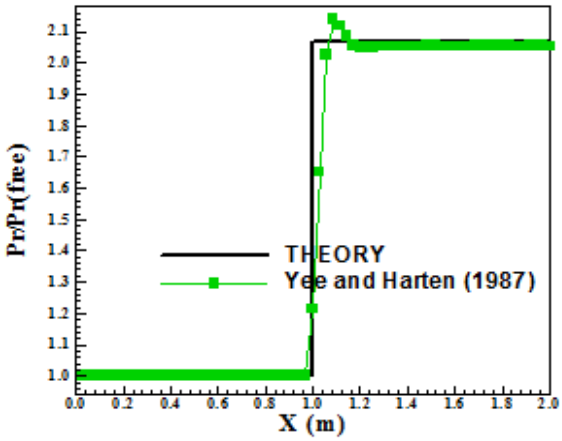

Figure 23. Wall pressure distribution ([12]).

Figure 22 presents the Mach number field generated by the [12] scheme. Good homogeneity

properties are observed. Non oscillations are observed in this solution.

Figure 23 shows the wall pressure distribution generated by the [12] TVD2 scheme. This solution presents a pressure peak at the discontinuity which damages its quality. Even so, the shock wave is captured with four (4) cells, which is a good result for a high resolution scheme.

10.2.2 Yang's second order results

Figures (24-25) show the pressure contours obtained by the [21] scheme, in its TVD and ENO second order accurate versions. Both solutions are free of oscillations, presenting a good transition between smooth and discontinuity regions.

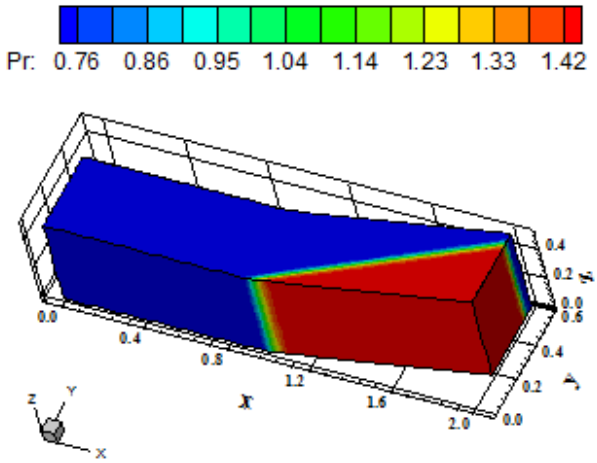

Figure 24. Pressure contours ([21]-TVD2).

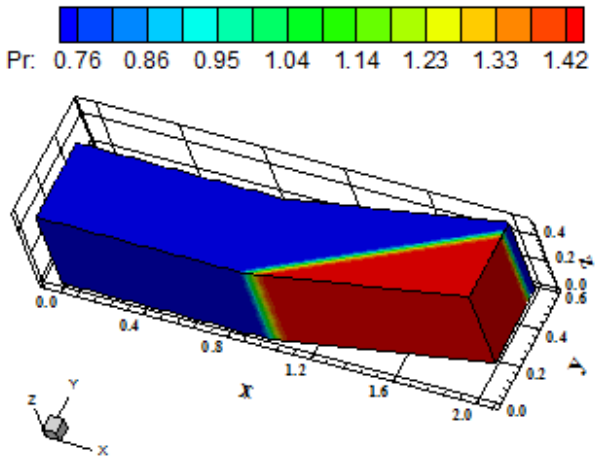

Figure 25. Pressure contours ([21]-ENO2).

In Figures (26-27) are exhibit the Mach number contours obtained by the [21] algorithm in its TVD2 and ENO2 versions. As can be seen, no oscillations are present in the solutions. The Mach number homogeneity properties are well assured by the solution algorithm.

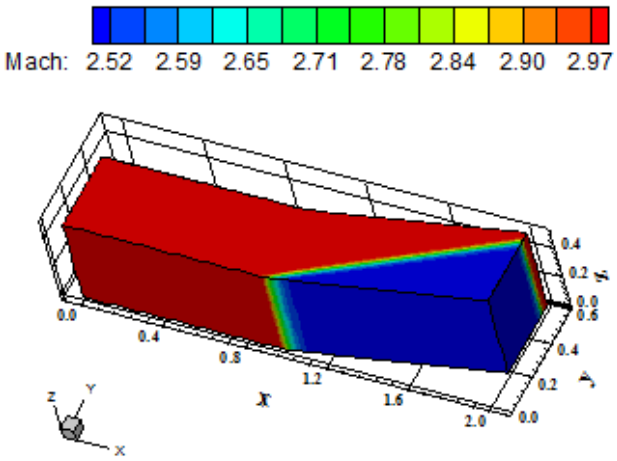

Figure 26. Mach number contours ([21]-TVD2).

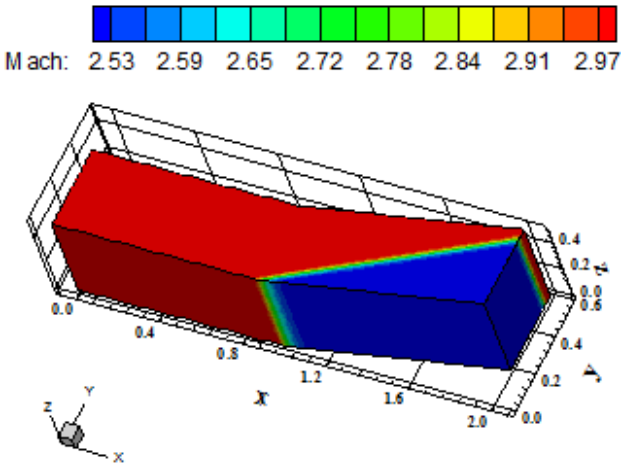

Figure 27. Mach number contours ([21]-ENO2).

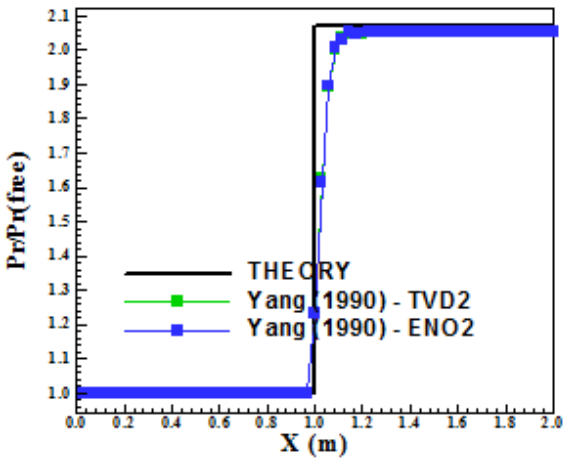

Figure 28. Wall pressure distributions ([21]).

Figure 28 shows the wall pressure distributions obtained by the two versions of the [21] algorithm. They are compared with the oblique shock wave

theory results. As can be seen, the [21] algorithms in its ENO2 version presents slightly better behavior than the TVD2 version. The pressure plateau is well characterized by both algorithms. The shock discontinuity is captured using five (5) cells, which is prejudicial in the solution quality and bad for a high resolution scheme. Typical number of cells is at maximum four (4).

10.2.3 Yang's third order results

Figures (29-30) exhibit the pressure contours obtained from [24], in its TVD and ENO versions of third-order accuracy, respectively. The solutions are free of oscillations and present good capture of shock discontinuity. The TVD3 version of the [24] algorithm presents the smallest shock wave thickness.

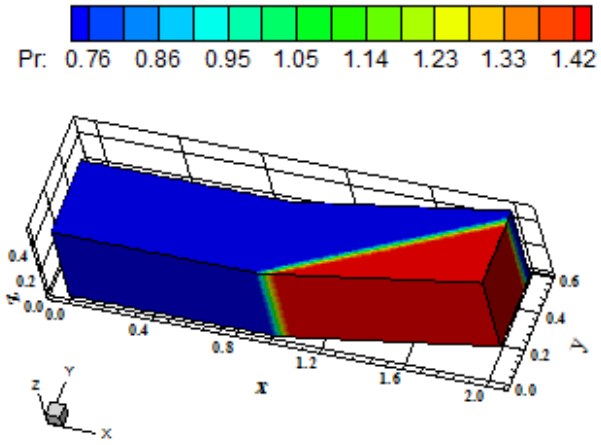

Figure 29. Pressure contours ([24]-TVD3).

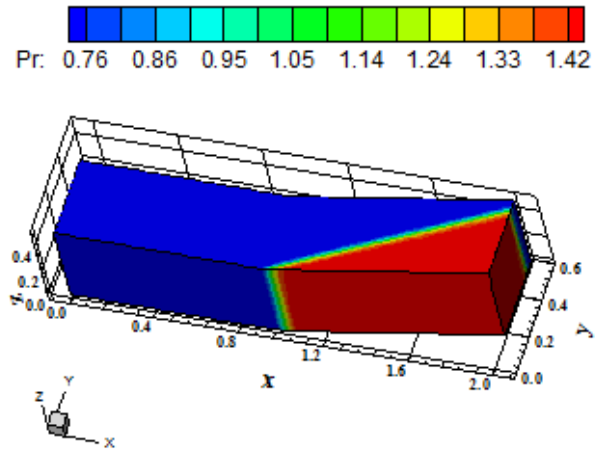

Figure 30. Pressure contours ([24]-ENO3).

Figures (31-32) show the Mach number contours obtained by [24] in its TVD3 and ENO3 versions. As can be seen, no oscillations are presented. Moreover, the homogeneity properties are obtained and the Mach number peak accords to the freestream Mach number.

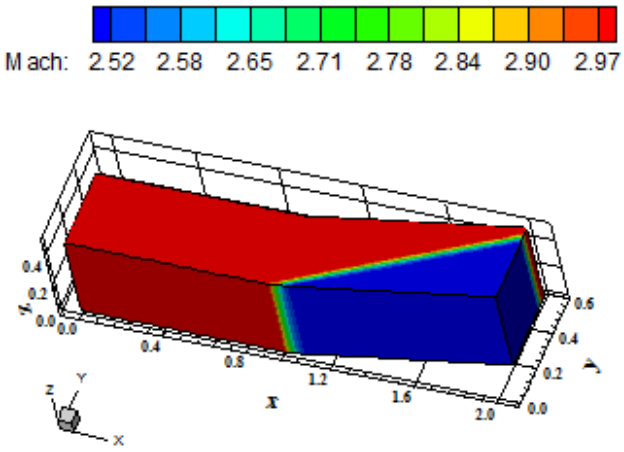

Figure 31. Mach number contours ([24]-TVD3).

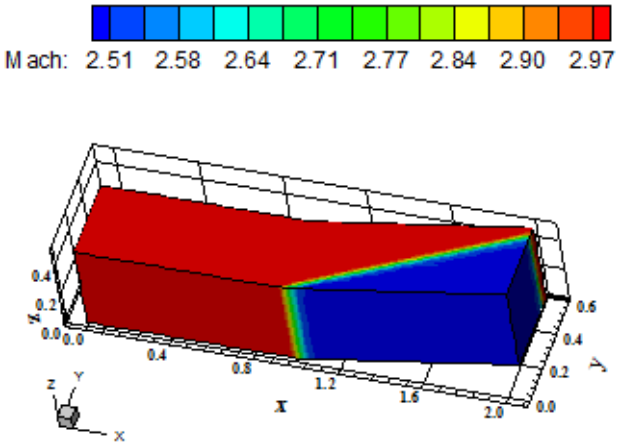

Figure 32. Mach number contours ([24]-ENO3).

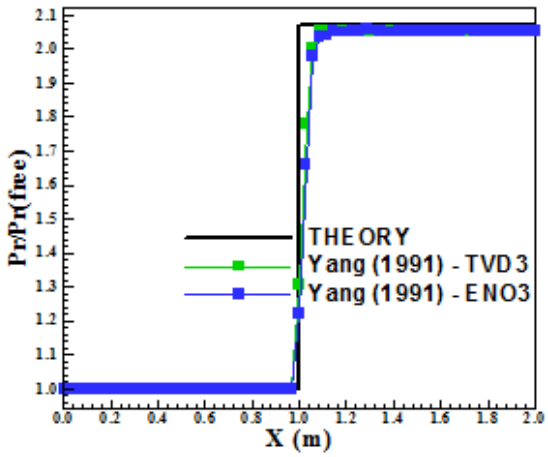

Figure 33. Wall pressure distributions ([24]).

Figure 33 presents the wall pressure distributions obtained by the two versions of the [24] algorithm.

As can see, both solutions are very close. However, it is possible to distinguish that the ENO3 solution is closer to the theory profile at the shock region and that it allows a smoother transition in the shock region, presenting no overshoots and undershoots. The shock profile is captured using four (4) cells.

10.2.4 Yang and Hsu's third order results

Figure 34 exhibits the pressure contours resulting from the [25] UNO3 scheme. As can be seen, no oscillations and good capture of the shock discontinuity are observed.

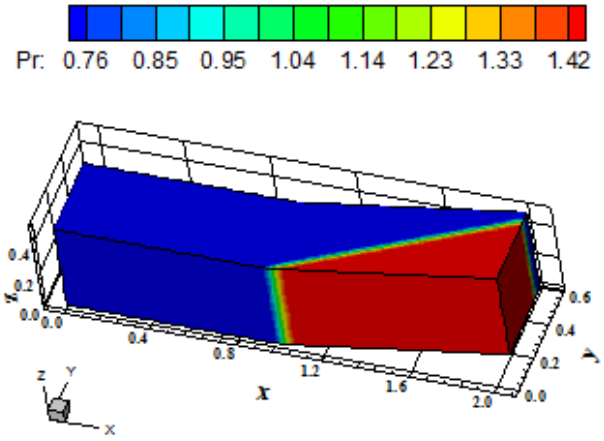

Figure 34. Pressure contours ([25]-UNO3).

Figure 35 presents the Mach number contours generated by the [25] UNO3 algorithm. This scheme captures the shock discontinuity appropriately, without overshoots and undershoots. The freestream Mach number is preserved and the homogeneity properties are conserved.

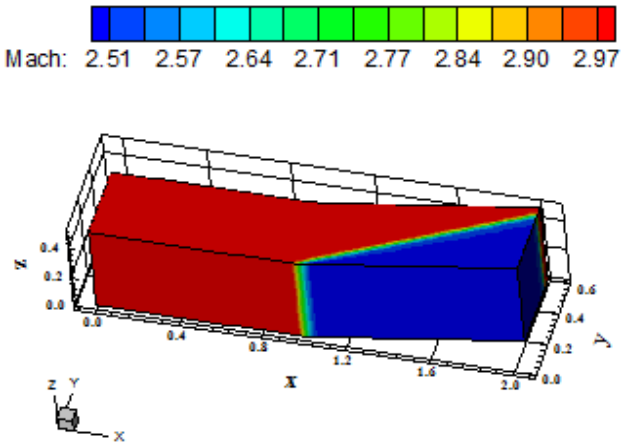

Figure 35. Mach number contours ([25]-UNO3).

Figure 36 shows the wall pressure distribution obtained by the [25] UNO3 scheme. The pressure discontinuity is captured using four (4) cells, which is a good result to a high resolution scheme. The shock profile is also close to the theoretical solution.

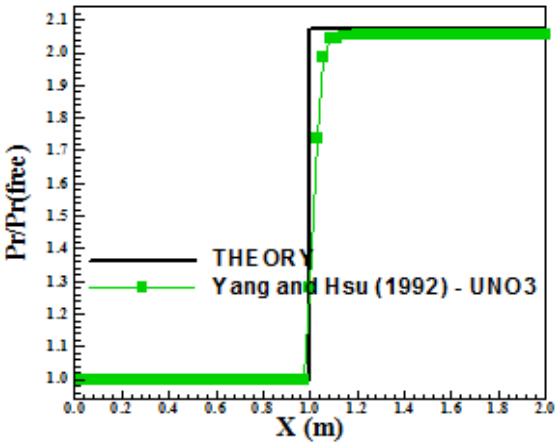

Figure 36. Wall pressure distributions ([25]).

Figure 37 shows the wall pressure distributions obtained by all schemes. They are compared with the oblique shock wave theory results. The best solution is that obtained with the [25] UNO3 scheme.

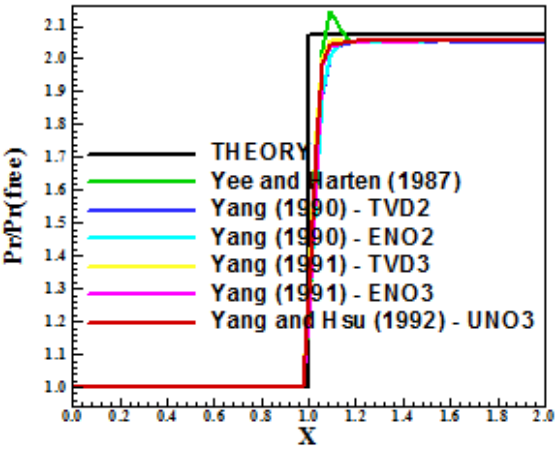

Figure 37. Wall pressure distributions (Global).

The value of the shock angle of the oblique shock wave at the compression corner is determined as function of the freestream Mach number and of the deflection angle of the flow after the shock wave, ϕ. To the compression corner problem, $\phi = 10°$ (ramp inclination angle) and the freestream Mach number is 3.0, resulting from this diagram a value to β equals to 27.5°. Using a transfer in the pressure contours figures, at the xy plane, it is possible to obtain the values of β to each scheme, as well the respective errors, shown in Tab. 2. As can be

observed, the [25] UNO3 algorithm has yielded the best results. Errors less than 5.50% were observed in all solutions.

Table 2. Shock angle and percentage errors.

Algotithm	β (°)	Error (%)
[12] – TVD2	27.0	1.82
[21] – TVD2	26.0	5.45
[21] – ENO2	27.0	1.82
[24] – TVD3	27.0	1.82
[24] – ENO3	27.0	1.82
[25] – UNO3	27.4	0.36

10.3 Ramp Problem – Viscous

The ramp configuration is described in Fig. 1. The ramp inclination angle is 20^o. An algebraic mesh of 61x60x10 points or composed of 31,860 hexahedrons and 36,600 nodes was used as shown in Fig. 38. An exponential stretching was used in the η direction to capture viscous effects.

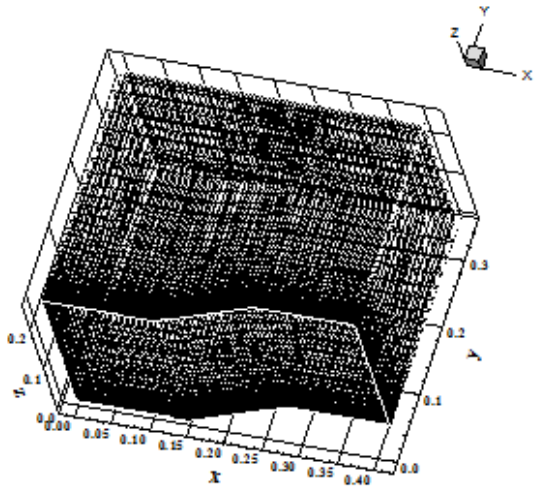

Figure 38. Ramp mesh (61x60x10).

This problem consists in a low supersonic flow impinging a ramp, where an oblique shock wave and an expansion fan are generated. Viscous effects are captured by the present Navier-Stokes formulation. The freestream Mach number is equal to 2.0. The solutions are compared with the oblique shock wave theory and the Prandtl-Meyer expansion fan theory, which are valid to comparison based on the boundary layer theory.

10.3.1 Yee and Harten's results

Figure 39 shows the pressure contours obtained by the [12] TVD2 scheme. As can be seen, the increase of the boundary layer thickness close to the ramp beginning originates a detachment of this layer, generating a separation and the formation of a circulation bubble at the corner. A weak shock wave ahead of the corner beginning is formed, which interacts with the expected oblique shock at the ramp.

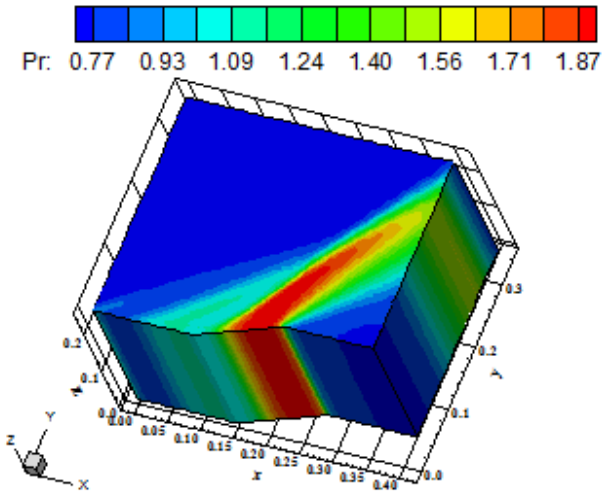

Figure 39. Pressure contours ([12]-TVD2).

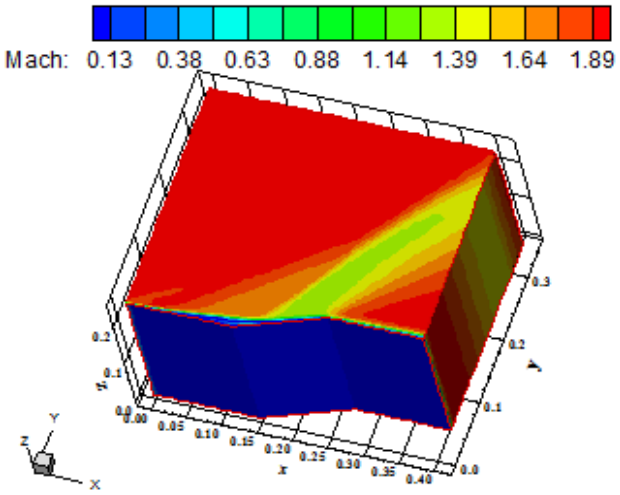

Figure 40. Mach number contours ([12]-TVD2).

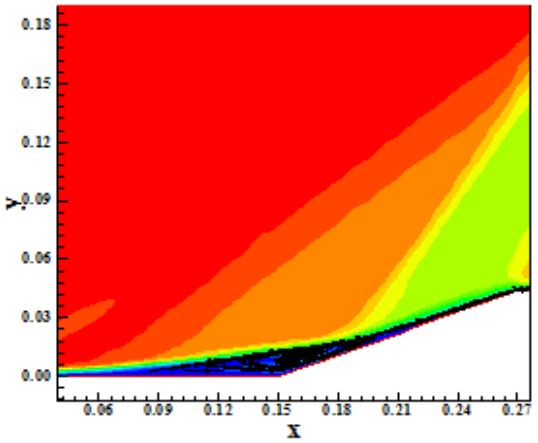

Figure 41. Circulation bubble formation ([12]-TVD2).

Figure 40 exhibits the Mach number contours generated by the [12] TVD2 scheme. As can be seen, a region of circulation is formed close to the corner wall.

Figure 41 presents the circulation bubble formed at the corner wall. It is possible to see the boundary layer detachment and reattachment.

Figure 42 shows the wall pressure distribution generated by the [12] TVD2 scheme. It presents the region of separation by a minor pressure peak ahead of the ramp. The shock at the ramp is well captured by the scheme. It is represented by the second pressure peak, which appears at the ramp region. The smooth characteristic of this shock is due to viscous effects.

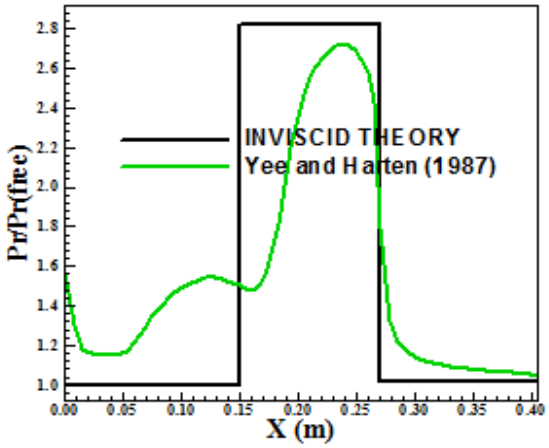

Figure 42. Wall pressure distribution ([12]).

10.3.2 Yang's second order results

Figures (43-44) show the pressure contours obtained by the [21] scheme, in its TVD and ENO second order accurate versions. As can see, the non-homogeneity in both solutions characterizes the loose of three-dimensional properties.

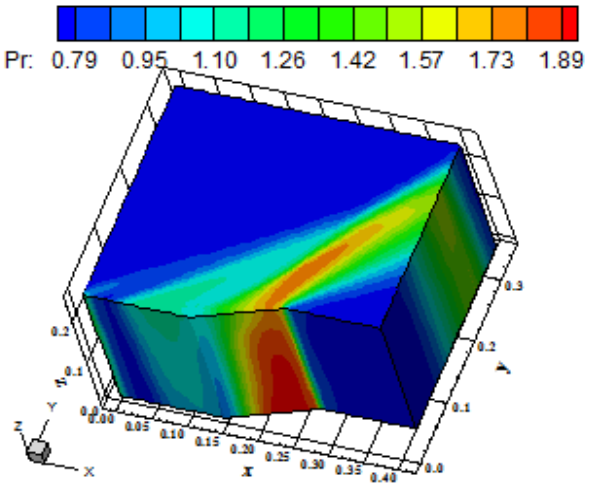

Figure 43. Pressure contours ([21]-TVD2).

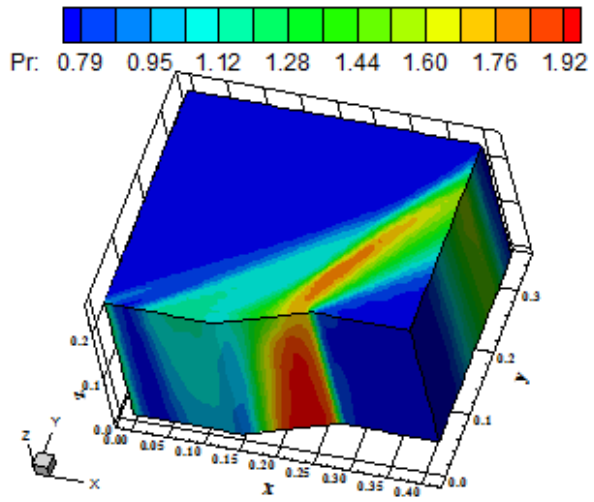

Figure 44. Pressure contours ([21]-ENO2).

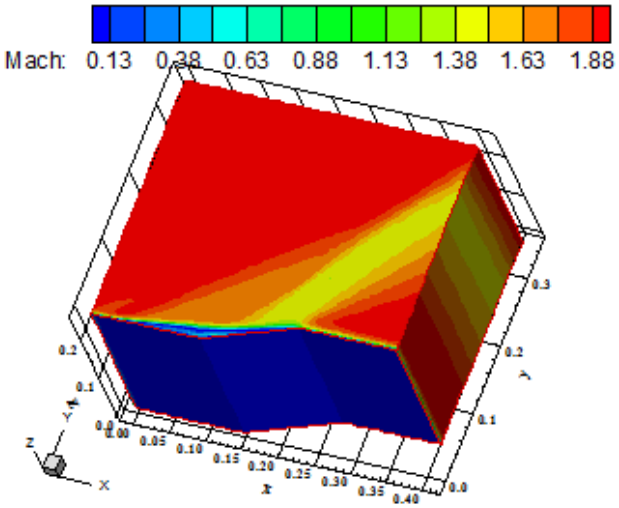

Figure 45. Mach number contours ([21]-TVD2).

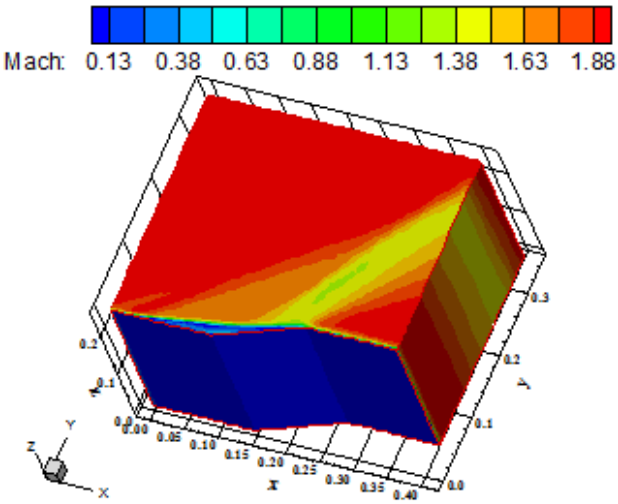

Figure 46. Mach number contours ([21]-ENO2).

It is important to emphasize here that the [21] scheme, as also [24-25] were designed to yield good solutions to hyperbolic equations like the Euler

equations. In the viscous case, the loose of quality in the solutions is due to a non-appropriate capture of the viscous effects.

Figures (45-46) exhibit the Mach number contours obtained by the [21] scheme in its TVD and ENO versions, respectively. The region of separation is well characterized in both solutions. Figures (47-48) presents the circulation bubble formation close to the corner wall. Both schemes capture appropriately the circulation bubble.

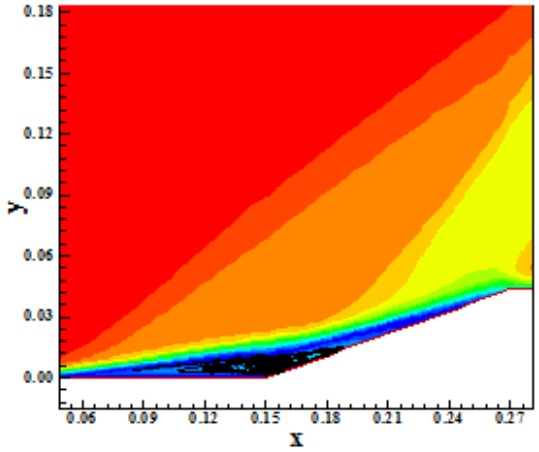

Figure 47. Circulation bubble formation ([21]-TVD2).

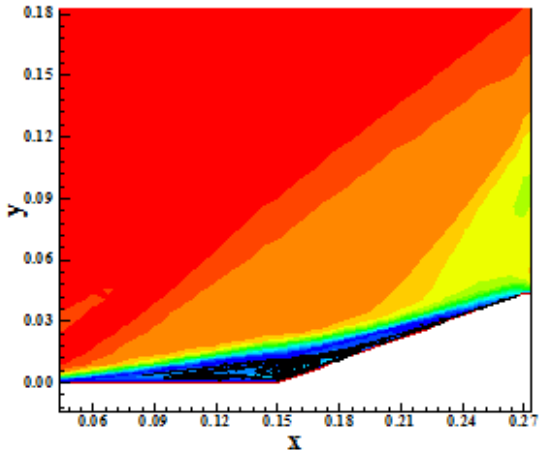

Figure 48. Circulation bubble formation ([21]-ENO2).

Figure 49 shows the wall pressure distributions generated by the [21] scheme in its two versions: TVD2 and ENO2. They are compared with the oblique shock wave results and the Prandtl and Meyer expansion wave results. Both versions of [21] capture the weak and the strong shock waves at the ramp beginning and at the ramp. The ENO2 solution predicts a more severe strong shock wave than the TVD2 solution. It characterizes the ENO2 version of [21] as presenting a more conservative solution than the TVD2 version.

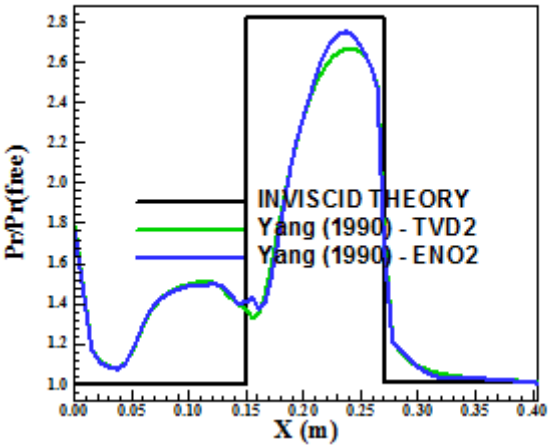

Figure 49. Wall pressure distributions ([21]).

10.3.3 Yang's third order results

Figure (50-51) exhibit the pressure contours obtained by [24] in its TVD3 and ENO3 versions.

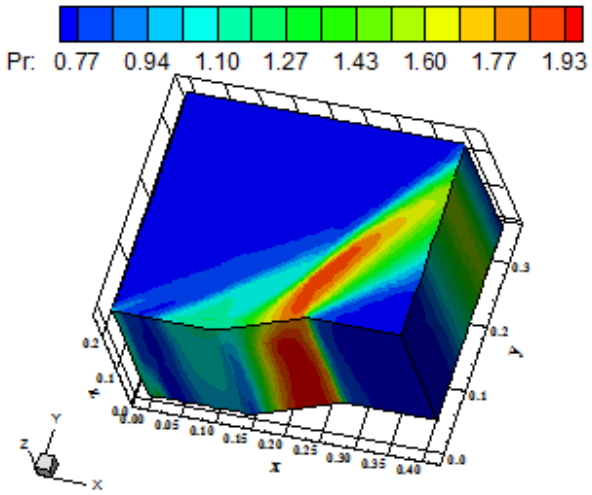

Figure 50. Pressure contours ([24]-TVD3).

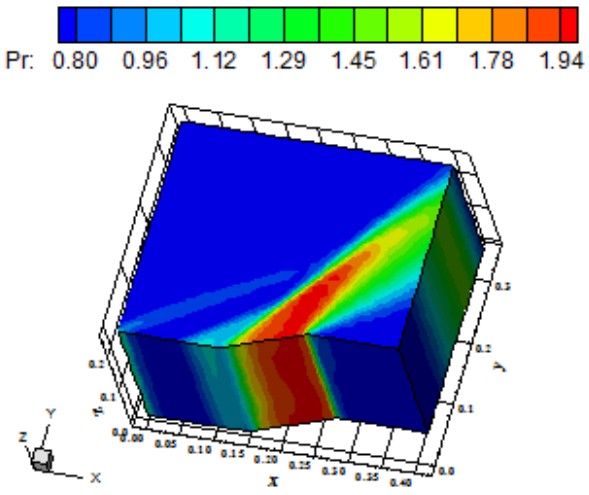

Figure 51. Pressure contours ([24]-ENO3).

As can be noted, pressure contours are not homogeneous solutions. The most severe pressure field is due to [24] in its ENO3 version.

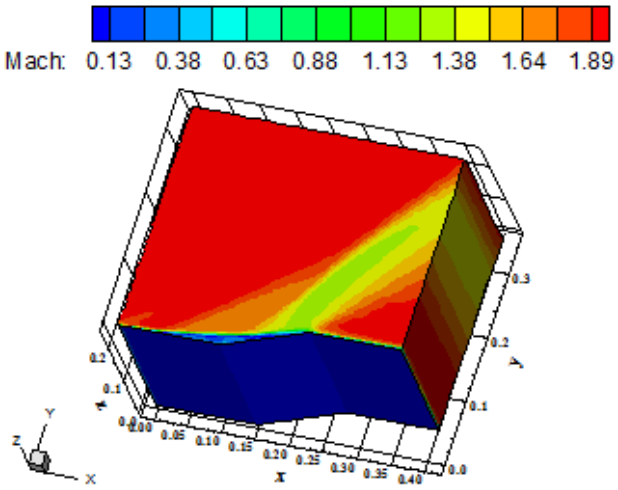

Figure 52. Mach number contours ([24]-TVD3).

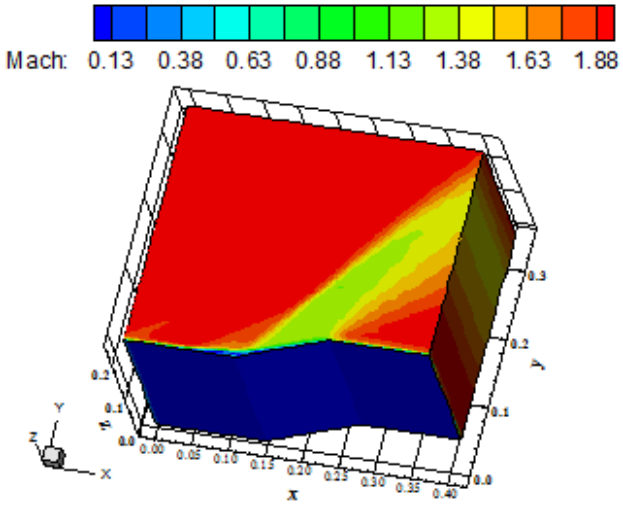

Figure 53. Mach number contours ([24]-ENO3).

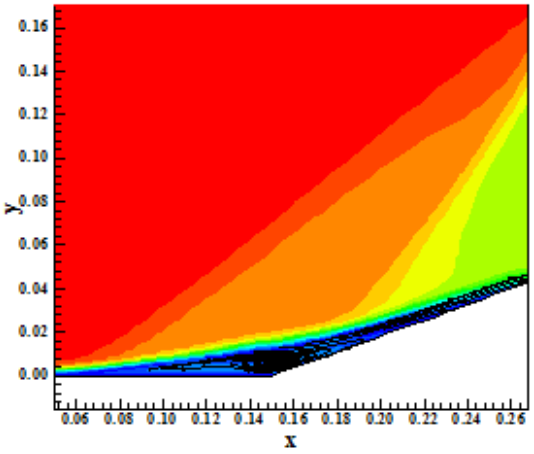

Figure 54. Circulation bubble formation ([24]-TVD3).

Figures (52-53) present the Mach number contours generated by the [24] scheme in its TVD3 and ENO3 versions. The circulation bubble is well captured by both versions. The boundary layer detachment and reattachment region is larger in the TVD3 solution.

Figures (54-55) show the circulation bubble formation at the separation region captured by [24] scheme in its TVD3 and ENO3 versions. As said before, the separation region generated by the [24]-TVD3 scheme is larger than that obtained with [24]-ENO3 scheme. Both versions of the [24] scheme capture the circulation bubble.

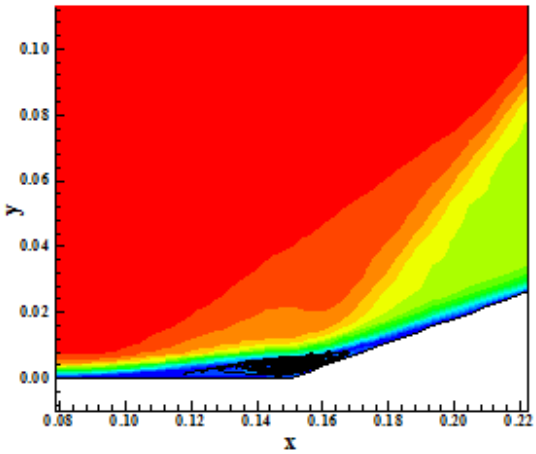

Figure 55. Circulation bubble formation ([24]-ENO3).

Figure 56 exhibits the wall pressure distributions generated by the [24] scheme in its TVD3 and ENO3 variants. They are compared with the oblique shock wave results and the Prandtl and Meyer expansion wave results. Both versions of [24] capture the weak and the strong shock waves at the ramp beginning and at the ramp. Both profiles predict approximately the same pressure peak at the ramp region.

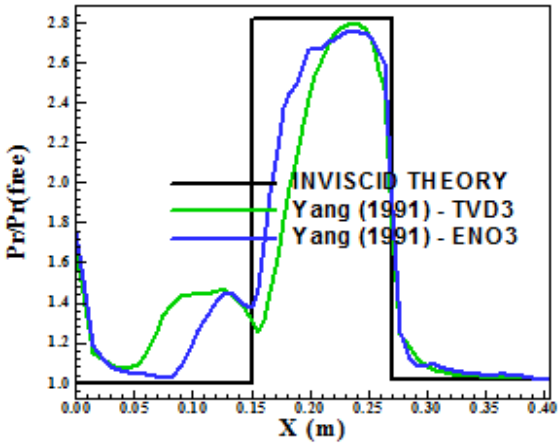

Figure 56. Wall pressure distributions ([24]).

As can be seen, the separation region in the TVD3 version of [24] scheme, before the ramp, is more extent than the respective one of the ENO3 version of [24], as noted before.

10.3.4 Yang and Hsu's second order results

Figures 57 shows the pressure contours obtained by the [25] scheme. The contours present good homogeneity properties. The shock is well captured. Figure 58 exhibits the Mach number contours obtained by the [25] scheme. The circulation bubble is well characterized in the Mach number contours. Figure 59 highlights the circulation bubble formation, in terms of streamlines, in the Mach number contours.

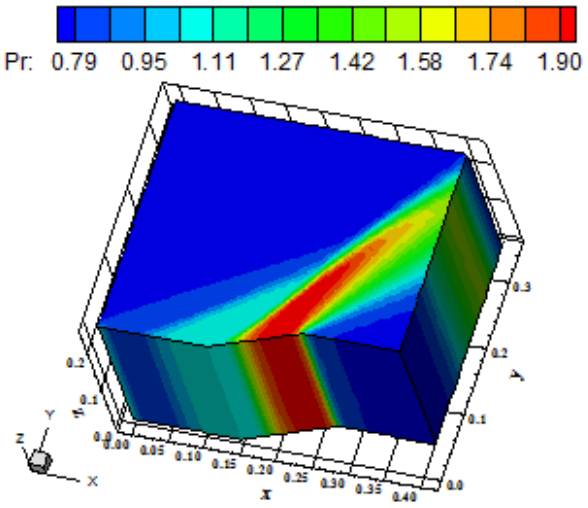

Figure 57. Pressure contours ([25]).

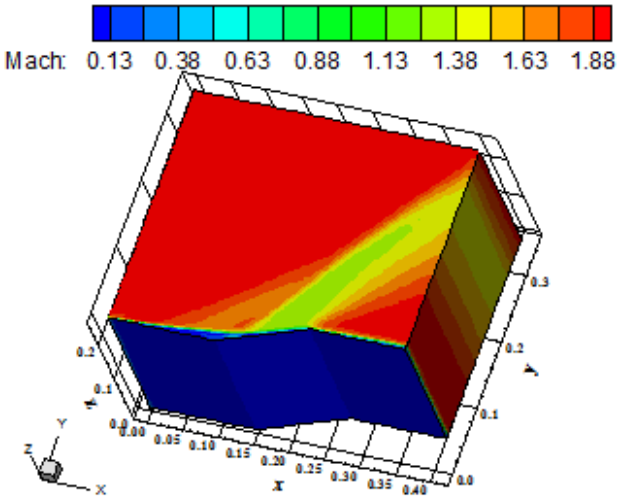

Figure 58. Mach number contours ([25]).

Figure 60 presents the wall pressure distribution obtained by the [25] scheme. It is compared with the oblique shock wave results and the Prandtl and Meyer expansion wave results. The boundary layer separation is well detected in this figure, represented by the first pressure peak, weaker than the ramp pressure peak. The pressure distribution presents a pressure peak close to the inviscid result, which is the correct solution considering the boundary layer theory.

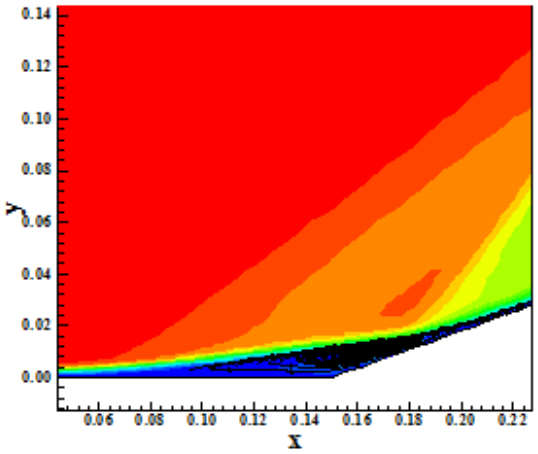

Figure 59. Circulation bubble formation ([25]).

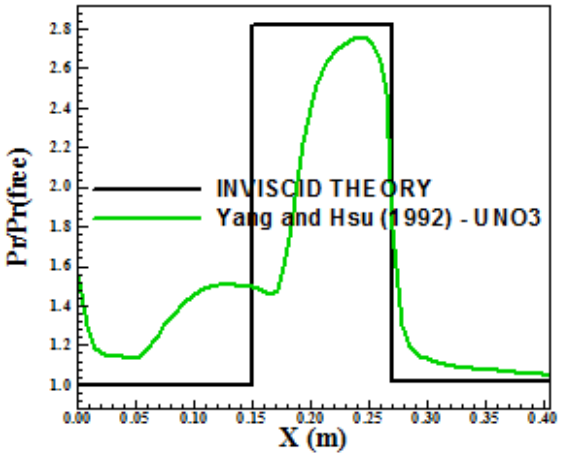

Figure 60. Wall pressure distribution ([25]).

10.4 Conclusion of this work

Concluding this analyze, the best algorithm was the [25] UNO3 scheme, presenting good pressure distributions in the ramp and compression corner problems, in the inviscid case. Moreover, this scheme also presented the best value to the shock angle of the oblique shock wave in the ramp problem, with 0.00% of error, and in the compression corner problem, with 0.36% of error. In the ramp viscous problem, good solutions are obtained with [25] algorithm, appropriating capturing the shock wave and the circulation bubble formation, close to the corner. Hence, this algorithm is the selected one to describe the two physical

problems studied herein, as comparing these six (6) numerical schemes.

10.5 Conclusion of this study

Comparing the results obtained in this work with those obtained in the first part of this study, it is possible to conclude that the [25] UNO3 algorithm is the best as involving all thirteen (13) schemes studied in Part I and the six (6) schemes studied herein. The smooth pressure distributions at the ramp and compression corner problems, in the inviscid case, rendered the distinction of best algorithm to the UNO3 one. In the viscous problem, although the first algorithms of Part I of this study have reached convergence with the convergent-divergent nozzle problem and the present ones did not, the latters are good described by the ramp problem. In the viscous ramp problem, both [12] and [25] schemes present good behavior, with a little better description by the [25] scheme. So, the better choice for these problems (ramp and compression corner inviscid problems and ramp and convergent-divergent nozzle viscous problems) is due to the [25] algorithm.

11 Conclusion

In the present work, second part of this study, the [12] TVD, the [21] TVD/ENO, the [24] TVD/ENO, and the [25] UNO schemes are implemented, on a finite volume context and using a structured spatial discretization, to solve the Euler and Navier-Stokes equations in the three-dimensional space. All schemes are high resolution flux difference splitting ones, based on the concept of Harten's modified flux function. The [12] is a TVD second order accurate in space and first order accurate in time algorithm. [21] is a TVD/ENO second order accurate in space and first order accurate in time algorithm. The [24] is a TVD/ENO third order accurate in space and first order accurate in time algorithm. Finally, the [25] is a UNO third order accurate in space and first order accurate in time algorithm. An implicit formulation is employed to solve the Euler equations. A Linearized Nonconservative Implicit LNI form or an approximate factorization ADI method is employed by the schemes. The algorithms are accelerated to the steady state solution using a spatially variable time step, which has demonstrated effective gains in terms of convergence rate ([32-33]). All schemes are applied to the solution of physical problems of the supersonic flows along a ramp and along a compression corner, in the inviscid case. The results have demonstrated that the [25] UNO algorithm, third order accurate in space, has presented the best solutions, in the two works of this study.

References:

[1] A. Harten, A High Resolution Scheme for the Computation of Weak Solutions of Hyperbolic Conservation Laws, *Journal of Computational Physics*, Vol. 49, 1983, pp. 357-393.

[2] A. Harten, On a Class of High Resolution Total-Variation-Stable Finite Difference Schemes, *SIAM Journal of Numerical Analysis*, Vol. 21, 1984, pp. 1-23.

[3] B. Van Leer, Towards the Ultimate Conservative Difference Scheme. V. A Second-Order Sequel to Godunov's Method, *Journal of Computational Physics*, Vol. 32, 1979, pp. 101-136.

[4] P. Colella, and P. R. Woodward, The Piecewise-Parabolic Method (PPM) for Gas-Dynamical Simulations, *LBL Rept. 14661*, July, 1982.

[5] P. L. Roe, Some Contributions to the Modelling of Discontinuous Flows, *Lectures in Applied Mathematics*, Vol. 22, Pt. II, 1985, pp. 163-193.

[6] S. Osher, Shock Modelling in Transonic and Supersonic Flow, *Recent Advances in Numerical Methods in Fluids*, Vol.4, *Advances in Computational Transonics*, edited by W. G. Habashi, Pineridge Press, Swansea, U. K., 1985.

[7] H. C. Yee, Generalized Formulation of a Class of Explicit and Implicit TVD Schemes, *NASA TM-86775*, 1985.

[8] P. L. Roe, Generalized Formulation of TVD Lax-Wendroff Schemes, *ICASE Rept. 84-53*, Oct., 1984.

[9] S. F. Davis, TVD Finite Difference Schemes and Artificial Viscosity, *ICASE Rept. 84-20*, June, 1984.

[10] H. C. Yee, On the Implementation of a Class of Upwind Schemes for Systems of Hyperbolic Conservation Laws, *NASA TM 86839*, September, 1985.

[11] H. C. Yee, R. F. Warming, and A. Harten, Implicit Total Variation Diminishing (TVD) Schemes for Steady-State Calculations, *Journal of Computational Physics*, Vol. 57, 1985, pp. 327-360.

[12] H. C. Yee, and A. Harten, Implicit TVD Schemes for Hyperbolic Conservation Laws in Curvilinear Coordinates, *AIAA Journal*, Vol. 25, No. 2, 1987, pp. 266-274.

[13] A. Harten, and S. Osher, Uniformly High Order Accurate Non-Oscillatory Schemes, I, *SIAM J. Num. Anal.*, Vol. 24, No. 2, 1987, pp. 279-309.

[14] A. Harten, B. Engquist, S. Osher, and S. R. Chakravarthy, Some results on Uniformly High-Order Accurate Essentially Non-Oscillatory Schemes, *Advances in Numerical Analysis and Applied Mathematics*, edited by J. C. South, Jr. and M. Y. Hussaini, *ICASE Rept. 86-18*, 1986; also *Journal of Applied Num. Mathematics*, Vol. 2, 1986, pp. 347-367.

[15] A. Harten, B. Engquist, S. Osher, and S. R. Chakravarthy, Uniformly High Order Accurate Essentially Non-Oscillatory Schemes, III, *ICASE Rept. 86-22*, 1986.

[16] S. K. Godunov, A Finite Difference Method for the Numerical Computation of Discontinuous Solutions of the Equations to Fluid Dynamics, *Math. Sb.*, Vol. 47, 1958, pp. 271-290.

[17] P. Colella, and P. R. Woodward, The Piecewise-Parabolic Method (PPM) for Gas-Dynamical Simulations, *Journal of Computational Physics*, Vol. 54, No. 1, 1984, pp. 174-201.

[18] A. Harten, High Resolution Schemes for Hyperbolic Conservation Laws, *Journal of Computational Physics*, Vol. 49, No. 3, 1983, pp. 357-393.

[19] P. K. Sweby, High Resolution Schemes Using Flux Limiters for Hyperbolic Conservation Laws, *SIAM Journal of Numerical Analysis*, Vol. 21, No. 5, 1984, pp. 995-1011.

[20] E. S. G. Maciel, Explicit and Implicit TVD High Resolution Schemes in 2D, *WSEAS Transactions on Applied and Theoretical Mechanics*, Vol. 7, No. 3, 2012, pp. 182-209.

[21] J. Y. Yang, Uniformly Second-Order-Accurate Essentially Non-oscillatory Schemes for the Euler Equations, *AIAA Journal*, Vol. 28, No. 12, 1990, pp. 2069-2076.

[22] J. Y. Yang, C. K. Lombardi, and D. Bershader, Numerical Simulation of Transient Inviscid Shock Tube Flows, *AIAA Journal*, Vol. 25, No. 2, 1987, pp. 245-251.

[23] J. Y. Yang, Y. Liu, and H. Lomax, Computation of Shock-Wave Reflection by Circular Cylinder, *AIAA Journal*, Vol. 25, No. 5, 1987, pp. 636-689.

[24] J. Y. Yang, Third-Order Nonoscillatory Schemes for the Euler Equations, *AIAA Journal*, Vol. 29, No. 10, 1991, pp. 1611-1618.

[25] J. Y. Yang, and C. A. Hsu, High Resolution, Nonoscillatory Schemes for Unsteady Compressible Flows, *AIAA Journal*, Vol. 30, No. 6, 1992, pp. 1570-1575.

[26] P. L. Roe, Approximate Riemann Solvers, Parameter Vectors, and Difference Schemes, *Journal of Computational Physics*, Vol. 43, No. 2, 1981, pp. 357-372.

[27] R. M. Beam, and R. F. Warming, An Implicit Factored Scheme for the Compressible Navier-Stokes Equations, *AIAA Journal*, Vol. 16, No. 4, 1978, pp. 393-402.

[28] J. Douglas, On the Numerical Integration of $u_{xx}+u_{yy}=u_t$ by Implicit Methods, *Journal of the Society of Industrial and Applied Mathematics*, Vol. 3, 1955, pp. 42-65.

[29] D. W. Peaceman, and H. H. Rachford, The Numerical Solution of Parabolic and Elliptic Differential Equations, *Journal of the Society of Industrial and Applied Mathematics*, Vol. 3, 1955, pp. 28-41.

[30] J. Douglas, and J. E. Gunn, A General Formulation of Alternating Direction Methods, *Numerische Mathematiks*, Vol. 6, 1964, pp. 428-453.

[31] N. N. Yanenko, *The Method of Fractional Steps*, Springer Verlag, N.Y., EUA, 1971.

[32] E. S. G. Maciel, Analysis of Convergence Acceleration Techniques Used in Unstructured Algorithms in the Solution of Aeronautical Problems – Part I, *Proceedings of the XVIII International Congress of Mechanical Engineering (XVIII COBEM)*, Ouro Preto, MG, Brazil, 2005. [CD-ROM]

[33] E. S. G. Maciel, Analysis of Convergence Acceleration Techniques Used in Unstructured Algorithms in the Solution of Aerospace Problems – Part II, *Proceedings of the XII Brazilian Congress of Thermal Engineering and Sciences (XII ENCIT)*, Belo Horizonte, MG, Brazil., 2008 [CD-ROM]

[34] R. W. Fox, and A. T. McDonald, *Introdução à Mecânica dos Fluidos*, Ed. Guanabara Koogan, Rio de Janeiro, RJ, Brazil, 632p, 1988.

[35] E. S. G. Maciel, TVD Algorithms Applied to the Solution of the Euler and Navier-Stokes Equations in Three-Dimensions, *WSEAS Transactions on Mathematics*, Vol. 11, June, Issue 6, 2012, pp. 546-572.

[36] E. S. G. Maciel, and A. P. Pimenta, Reentry Flows in Chemical Non-Equilibrium in Three-Dimensions, *WSEAS Transactions on Mathematics*, Vol. 11, March, Issue 3, pp. 227-256.

[37] G. Strang, On the Construction and Comparison of Difference Schemes, *SINUM*, Vol. 5, 1968, pp. 506-517.

[38] J. Y. Yang, Second- and Third-Order Upwind Flux Difference Splitting Schemes for the Euler Equations, *NASA TM-85959*, July, 1984.

[39] B.Van Leer,Towards the Ultimate Conservative Difference Scheme II, Monotonicity and Conservation Combined in a Second Order Scheme, *Journal of Computational Physics*, Vol. 14, No. 2, 1974, pp. 361-370.

[40] H. C. Yee, R. F. Warming, and A. Harten, A High-Resolution Numerical Technique for Inviscid Gas-Dynamic Problems with Weak Solutions, *Proceedings of the 8th International Conference on Numerical Methods in Fluid Dynamics*, E. Krause, Editor, *Lecture Notes in Physics*, Springer-Verlag, Berlim, Germany, Vol. 170, 1982, pp. 546-552.

[41] A. Jameson, and D. Mavriplis, Finite Volume Solution of the Two-Dimensional Euler Equations on a Regular Triangular Mesh, *AIAA Journal*, Vol. 24, 1986, pp. 611-618.

[42] E. S. G. Maciel, Simulação Numérica de Escoamentos Supersônicos e Hipersônicos Utilizando Técnicas de Dinâmica dos Fluidos Computacional, *Doctoral Thesis*, ITA, CTA, São José dos Campos, SP, Brazil, 258p, 2002.

[43] J. T. Batina, Implicit Upwind Solution Algorithms for Three-Dimensional Unstructured Meshes, *AIAA Journal*, Vol. 31, No. 5, 1993, pp. 801-805.

[44] J. D. Anderson Jr., *Fundamentals of Aerodynamics*, McGraw-Hill, Inc., EUA, 563p, 1984.